NASA-CR-191222

PENNSTATE

(NASA-CR-191222) COMBUSTION OF LOX WITH H2(SUB g) UNDER SUBCRITICAL, CRITICAL, AND SUPERCRITICAL CONDITIONS AND EXPERIMENTAL OBSERVATION OF DENSE SPRAY AND MIXING OF IMPINGING JETS Semiannual Report, 1 Feb. - 31 Oct. 1992 (Pennsylvania State Univ.) 63 p

N93-16647

Unclas

G3/25 0137991

PROPULSION ENGINEERING RESEARCH CENTER

SEMI-ANNUAL REPORT

COMBUSTION OF LOX WITH HYDROGEN UNDER SUBCRITICAL, CRITICAL, AND SUPERCRITICAL CONDITIONS (Task 1)
and
EXPERIMENTAL OBSERVATION OF DENSE SPRAY AND MIXING OF LIQUID JETS EMANATING FROM DOUBLET INJECTORS (Task 2)

Prepared by: K. K. Kuo, W. H. Hsieh and F. B. Cheung
A. S. Yang, M. C. Kline, R. D. Woodward and J. J. Brown

TO
Mr. Klaus W. Gross, Code: EP 55
NASA: Marshall Space Flight Center
Huntsville, Alabama 35812

A UNIVERSITY SPACE ENGINEERING RESEARCH CENTER

November 1992

106 RESEARCH BUILDING EAST
UNIVERSITY PARK, PENNSYLVANIA 16801

SEMI-ANNUAL REPORT

Combustion of LOX with $H_{2(g)}$ Under Subcritical, Critical, and Supercritical Conditions (Task 1)

and

Experimental Observation of Dense Spray and Mixing of Impinging Jets (Task 2)

Submitted to

Mr. Klaus W. Gross
Code: EP 55
NASA: Marshall Space Flight Center
Huntsville, Alabama 35812

Prepared by

K. K. Kuo, W. H. Hsieh, A. S. Yang and J. J. Brown (Task 1)

K. K. Kuo, F. B. Cheung, R. D. Woodward, M. C. Kline (Task 2)

PROPULSION ENGINEERING RESEARCH CENTER
The Pennsylvania State University
University Park, PA 16802

November 1992

TABLE OF CONTENTS

TASK NO. 1 COMBUSTION OF LOX WITH $H_{2(g)}$ UNDER SUBCRITICAL, CRITICAL, AND SUPERCRITICAL CONDITIONS

TABLE OF CONTENTS (Cont'd)

TASK NO. 2 DENSE SPRAY AND MIXING OF LIQUID JETS EMANATING FROM DOUBLET INJECTORS

ACKNOWLEDGMENT

This research project has been funded by NASA-MSFC under Contract Number NAG8-174. The authors would like to thank Mr. Klaus W. Gross of MSFC for his encouragement and support. A part of this work was supported by the Propulsion Research Engineering Center at The Pennsylvania State University (PSU). The interest and support of Prof. Charles L. Merkle, Director of PERC, is also acknowledged. Valuable input from Mr. David T. Harrje, a specialist in liquid rocket propulsion, on supercritical combustion of LOX is deeply acknowledged.

LIST OF FIGURES - Task 1

LIST OF FIGURES - Task 2

NOMENCLATURE

$a,\ b$	= Constants in Redlich-Kwong equation of state
f	= Fugacity
N	= Total number of species
n_i	= Number of moles of species i
P	= Pressure
R_u	= Universal gas constant
r	= Coordinate in the transverse direction
T	= Temperature
$u,\ v$	= Velocity components in x and r direction
V	= Total volume
W	= Molecular weight
x	= Coordinate in the axial direction
X	= Mole fraction
Y	= Mass fraction
Z	= Compressibility factor

Greek Symbols

ρ	= Density
ω	= Acentric Factor

Superscripts

$(\ )^o$	= Ideal state
$(\bar{\ })$	= Partial molar quantity

Subscripts

$(\ )_i$	= Species i
$(\ )_o$	= Boundary conditions of surrounding purge flows
$(\ )_s$	= Surface value
$(\ )_+$	= Boundary conditions of the LOX surface

Task No. 1

COMBUSTION OF LOX WITH $H_{2(g)}$ UNDER SUBCRITICAL, CRITICAL, AND SUPERCRITICAL CONDITIONS

K. K. Kuo, W. H. Hsieh, A. S. Yang, and J. J. Brown
Propulsion Engineering Research Center
The Pennsylvania State University
University Park, PA 16802

1. INTRODUCTION

This semi-annual report summarizes the progress made during the period of February 1 to October 15, 1992, under Task 1 of the contract entitled "Combustion of LOX with $H_{2(g)}$ under Subcritical, Critical, and Supercritical Conditions."

The overall objective of this investigation is to achieve a better understanding of the combustion processes of liquid oxygen and gaseous hydrogen under subcritical, critical, and supercritical conditions. Specific objectives of the research program are:

1. To determine the evaporation- and burning-rate characteristics of LOX in hydrogen/helium environments under broad ranges of operating conditions;
2. To measure species concentration profile and surface temperature of LOX employing the gas chromatography and fine-wire thermocouples under non-reacting flow situations;
3. To perform a fugacity-based multicomponent thermodynamic phase equilibrium analysis for examining the high-pressure vapor-liquid equilibrium behavior at the liquid surface of LOX;
4. To formulate and solve a theoretical model for simulating the evaporation and combustion processes in a LOX/H_2/He system; and
5. To validate the theoretical model with the measured experimental data.

2. EXPERIMENTAL WORK

The scope of the experimental work performed during this reporting period falls into two major areas: (1) evaporation tests; and (2) combustion tests. The progress made in each subject area is discussed below.

2.1 Evaporation Tests

During the gasification and burning processes of LOX droplets inside a liquid rocket engine at near-critical and supercritical conditions, the effects of solubility of ambient gases in the liquid phase and variations of thermodynamic and transport properties are important. These effects can influence both evaporation and combustion characteristics of the droplet. Therefore, prior to the development of a complete combustion model, it is useful to examine the above effects under non-reacting situations. In the tests, the helium is employed to pressurize the system instead of hydrogen for safety considerations. The other reason for using helium is due to its very similar solubility features as hydrogen.

The progress made in evaporation tests includes:

- Calibration of electronic mass flowmeters.
- Design and installation of the gas sampling system.
- Determination of evaporation rates for LOX strand vaporizing in helium environments.
- Measurements of liquid surface temperature.
- Gas composition analysis using chromatography.

2.1.1 Calibration of Electronic Mass Flowmeters

In order to calibrate electronic mass flowmeters (OMEGA, FMA-874-V) used for mass consumption rate measurements of oxygen and helium, a calibration setup

was devised as shown in Fig. 1.1. The source of the calibration medium was an air bottle. The inlet and outlet pressure of mass flowmeters were maintained at 650 and 600 psig, respectively. The condition specified here corresponds the mid-point for the test range of pressure. An aluminum case diaphragm meter (American Meter, AL-425), with ±1% calibrated accuracy in the range of 5 to 100 percent rated flow capacity, was installed in line with the electronic mass flowmeter to measure the standard flow rate. Between the above two flowmeters, a line regulator was mounted to reduce the gas pressure. Results given in Figs. 1.2 and 1.3 show that the accuracy is ±2% full scale.

2.1.2 Surface Temperature and Oxygen Concentration Measurements

The surface temperature at the outlet of the LOX feeding tube was measured using a 75 μm Fe/Cu-Ni (J-type) fine-wire thermocouple. To reduce conduction errors, the thermocouple lead wires were placed along the liquid oxygen surface for a distance of over 30 wire diameters.

For the setup of species measurement shown in Fig. 1.4, a quartz micro-probe was used to sample the gas composition along the centerline above the LOX surface. The probe was fabricated from a 3 mm diameter quartz tube tapered down to a 25 μm orifice. For each test, a gas sampling chamber was vacuumed and then filled with the gas sample through the probe to a pressure level slightly above atmospheric pressure (typically, 3 psig). Subsequently, the gas sample was withdrawn from the gas sampling chamber through a vacuum pump and analyzed by a Varian model 3700 gas chromatograph (GC) with a thermal conductivity detector. In order to make a reproducible amount of sample and injection time, an air-actuated 10-port switching valve (Valco Instruments, Model A410UWT) was employed to control the injection of the gas sample into the GC column. In this study, a Supelco Molecular Sieve 5A, 45/60 mesh 3' × 1/8" stainless-steel column was installed in the GC. The

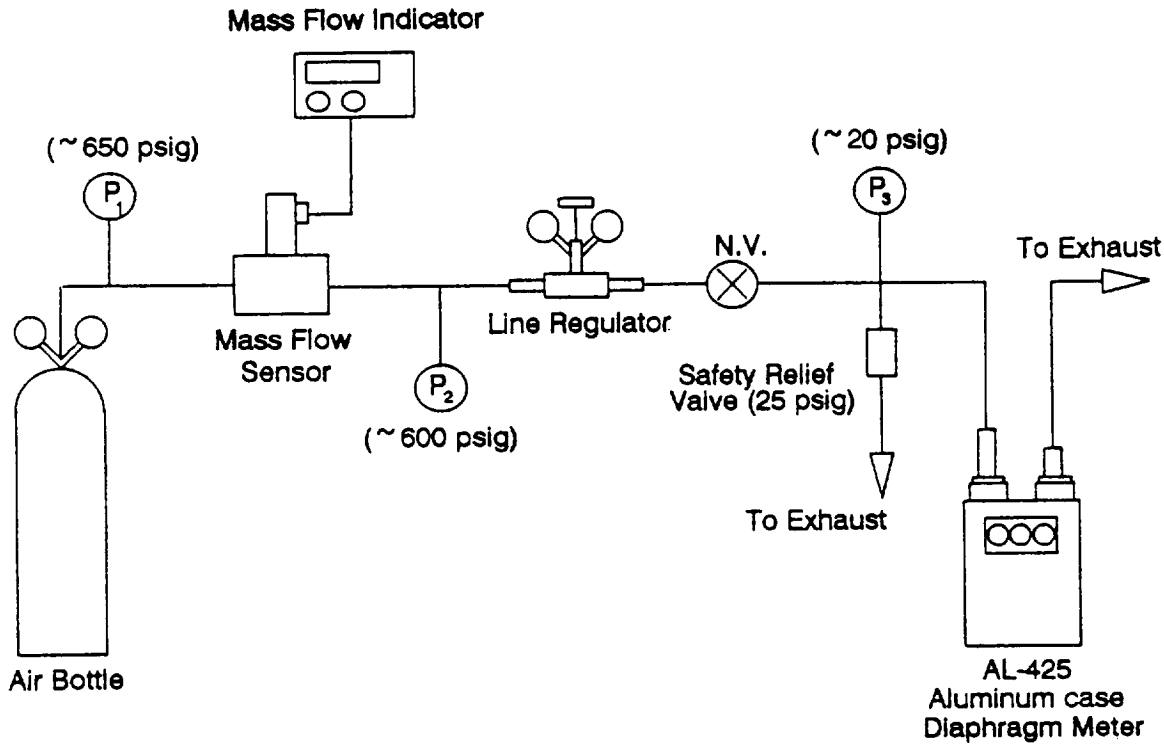

Figure 1.1 Schematic Diagram of the Apparatus Used for the Calibration of Mass Flowmeters

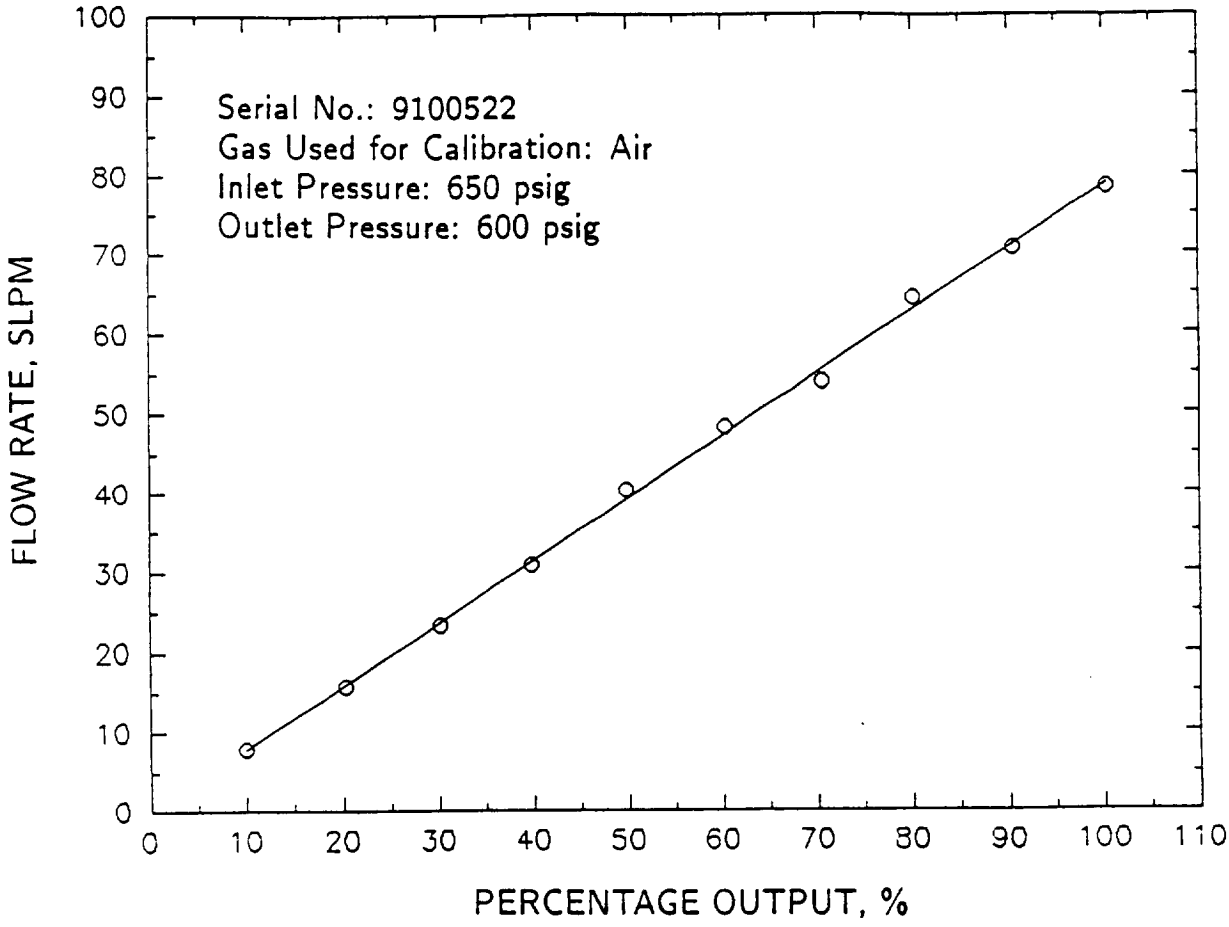

Figure 1.2 Calibration Curve of the Mass Flowmeter Used for the Oxygen Consumption Rate Measurement

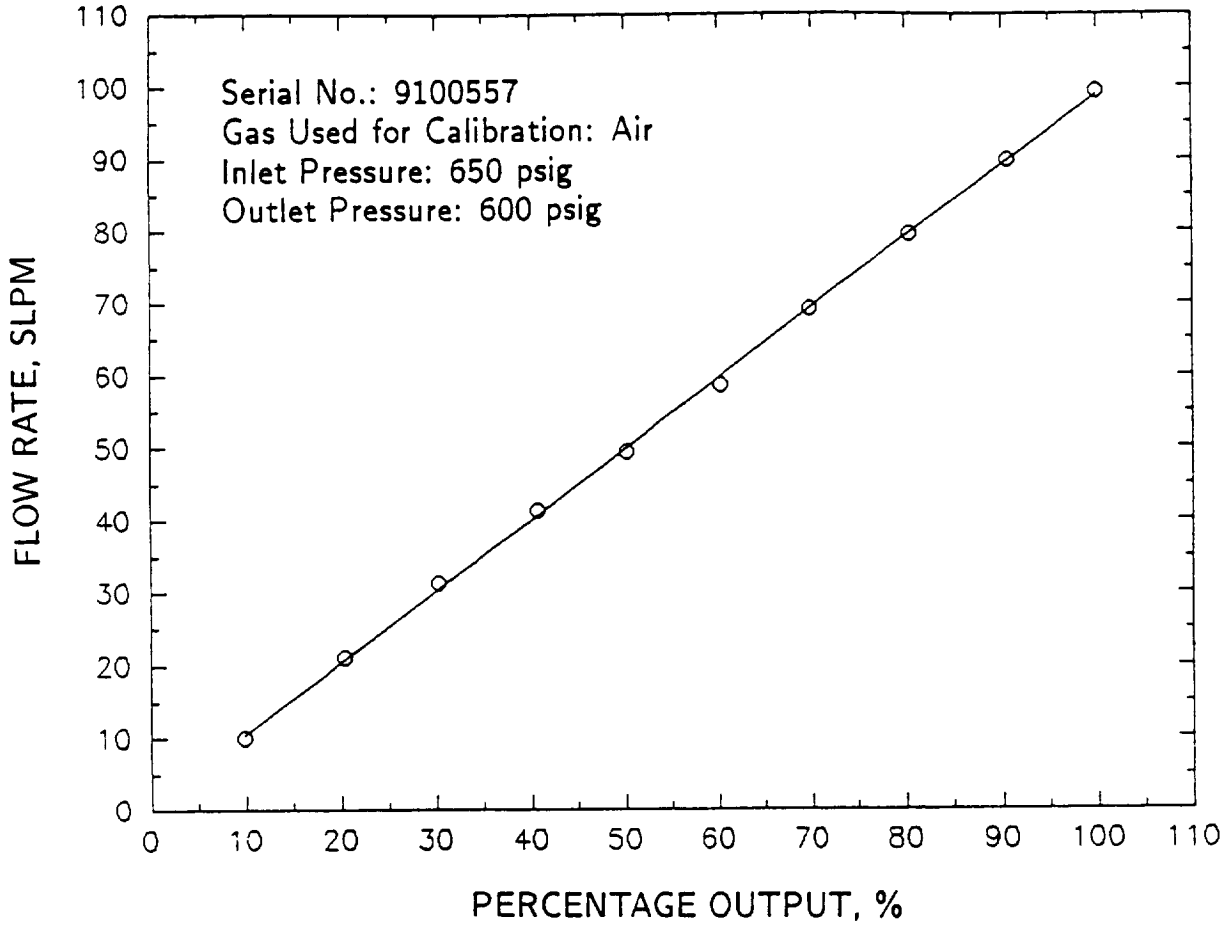

Figure 1.3 Calibration Curve of the Mass Flowmeter Used for the Helium Consumption Rate Measurement

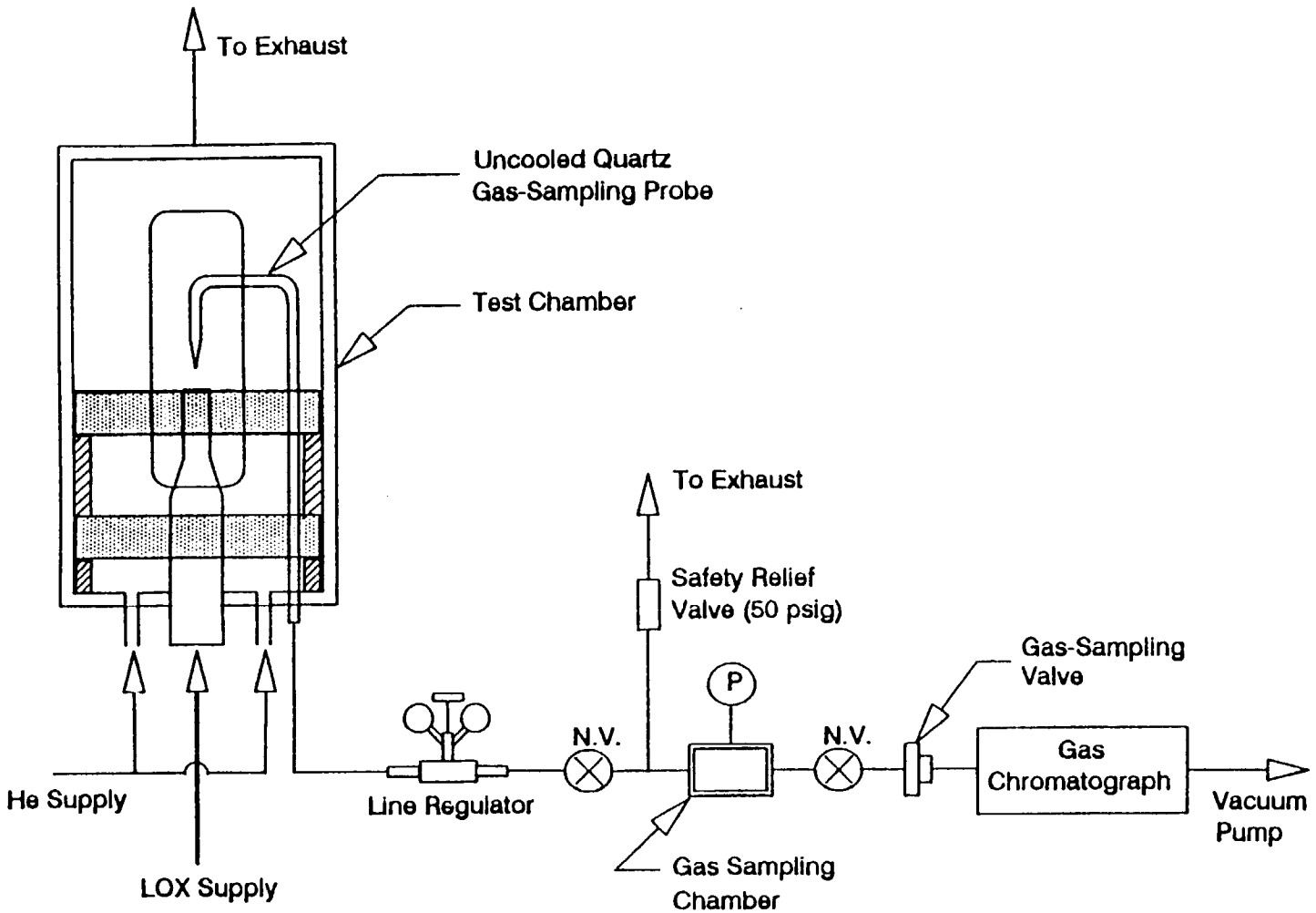

Figure 1.4 Schematic Diagram of the Apparatus Used for Oxygen Concentration Measurements

helium was employed as the carrier gas for the Molecular Sieve 5A column with the flow rare of 22 ml/min. In addition, following the same operation procedure described above, the GC was calibrated using known-concentration calibration gases. Details of chromatographic analysis can be found in Yeh's (1991) work.

2.2 Combustion Tests

Prior to the use of H_2/LOX system for combustion studies, a number of CH_4/GO_2 firing tests were carried out at atmospheric pressures to ensure the proper operation of the experimental setup. Figure 1.5 presents a picture of a stable methane/oxygen gaseous diffusion flame. The gaseous oxygen velocity at center tube was 0.5 m/sec with Reynolds number of 300. In addition, a combustion flame of LOX with methane has also been successfully established in the test chamber, as shown in Fig. 1.6. The current operational manual for evaporation tests has been updated to include the consideration of combustion tests. A detailed discussion of testing results will be given in the contract report.

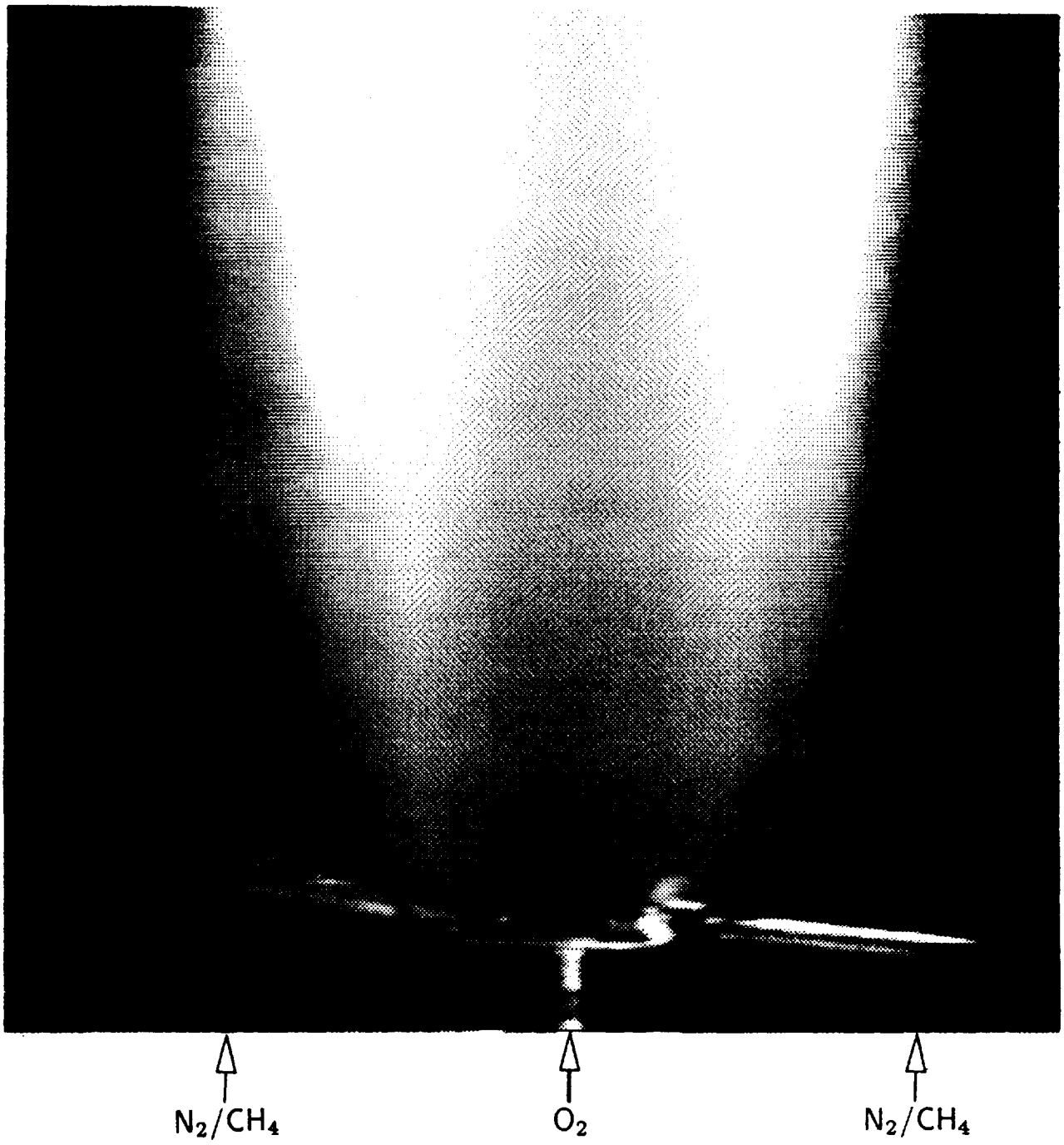

Figure 1.5 Picture of a Methane/Oxygen Diffusion Flame (Re = 300)

Figure 1.6 Picture of a Methane/LOX Diffusion Flame (Re = 75)

3. THEORETICAL WORK

The progress made in theoretical work is summarized as follows:

- Improvement of the high-pressure phase equilibrium model.
- Implementation of the numerical code for phase equilibrium calculations.
- Development of the computer code for flow analysis.
- Verification of the high-pressure phase equilibrium model.
- Verification of numerical solutions obtained from the flow analysis code.
- Cold flow simulations for studying the evaporation process in a LOX/He system.

3.1 Improvement of High-Pressure Phase Equilibrium Model

To obtain the species-concentration boundary conditions for each species immediately above the liquid surface, the thermodynamic phase equilibrium is imposed upon the gas/liquid interface. At low pressures, the dissolution of ambient gases in the liquid and the influence of pressure on thermophysical properties are negligible. The classical Raoult's law for ideal mixtures, therefore, can well define the phase equilibrium condition. However, in the high-pressure environments, fugacity-based multicomponent thermodynamic analysis for vapor-liquid phase equilibrium must be conducted to fully account for ambient gas solubility and real gas effects. The high-pressure vapor-liquid equilibria for each component can be expressed as follows:

$$f_i^{(v)} = f_i^{(l)} \tag{1}$$

$$T^{(v)} = T^{(l)} \tag{2}$$

$$P^{(v)} = P^{(l)} \tag{3}$$

where the superscripts (v) stands for vapor and (l) for liquid. The variable f_i is the fugacity for species i, and can be integrated through the following relation (Prausnitz *et al.*, 1986).

$$R_u T \; ln(\frac{f_i}{X_i P}) = \int_V^\infty \Big[\Big(\frac{\partial P}{\partial n_i} \Big)_{T,V,n_j} - \frac{R_u T}{V} \Big] dV - R_u T \; ln Z \tag{4}$$

where X_i and V are mole fraction of species i and total volume, respectively. The above equation indicates that f_i is determined by the properties of the constituent components, the concentrations in both phases, and the temperature and pressure of the system. To compute the integral form in Eq. (4), the Redlich-Kwong (R-K) equation of state is employed.

$$P = \frac{R_u T}{\bar{v} - b} - \frac{a}{\bar{v}(\bar{v} + b) T^{0.5}} \tag{5}$$

where $\bar{v}$ is the molar specific volume. The mixture parameters a, b in cubic-type equation of state can be expressed in terms of composition and pure component parameters.

$$a = \sum_{i=1}^{N} \sum_{j=1}^{N} X_i X_j a_{ij}, \qquad b = \sum_{i=1}^{N} X_i b_i \tag{6}$$

The constants a_{ij}, b_i are essentially dependent on the critical properties of each species. In addition, the quantum-gas mixing rule corrections must be made in this study to consider mixtures comprising one or more of the quantum gases (Prausnitz *et al.*, 1986).

$$\begin{aligned} a_{ii} &= \frac{0.42748 R_u^2 T_{c_i}^{2.5}}{P_{c_i}}, \\ a_{ij} &= \frac{0.42748 R_u^2 T_{c_{ij}}^{2.5}}{P_{c_{ij}}}, \\ b_i &= \frac{0.08664 R T_{c_i}}{P_{c_i}}. \end{aligned} \tag{7}$$

where

$$
\begin{aligned}
T_{c_{ij}} &= \frac{T^*_{c_{ij}}}{1+(c_1/W_{ij}T)}, \\
P_{c_{ij}} &= \frac{P^*_{c_{ij}}}{1+(c_2/W_{ij}T)}, \\
T^*_{c_{ij}} &= \sqrt{T_{c_i}T_{c_j}}(1-K_{ij}), \\
P^*_{c_{ij}} &= \frac{Z_{c_{ij}}R_u T^*_{c_{ij}}}{\bar{v}_{c_{ij}}}, \\
\bar{v}^{1/3}_{c_{ij}} &= (\bar{v}^{1/3}_{c_i}+\bar{v}^{1/3}_{c_j})/2, \\
Z_{c_{ij}} &= 0.291-0.04(\omega_i+\omega_j), \\
\frac{1}{W_{ij}} &= \left(\frac{1}{W_i}+\frac{1}{W_j}\right)/2, \\
K_{ij} &= 1-\frac{8(\bar{v}_{c_i}\bar{v}_{c_j})^{1/2}}{(\bar{v}^{1/3}_{c_i}+\bar{v}^{1/3}_{c_j})^3}.
\end{aligned}
\tag{8}
$$

Note that the values of c_1 and c_2 are 21.8 and 44.2, respectively. The critical properties and acentric factors of pure components employed in the analysis are given in Table 1.1 (Reid *et al.*, 1987). Because of the prevailing influence of the helium on the liquid surface behavior, only binary system containing oxygen and helium is considered in the phase equilibrium calculations. Moreover, instead of conventional critical constants, effective critical constants are required to implement the quantum-gas mixing rules. Table 1.2 lists the values of effective critical constants and acentric factor for the helium (Prausnitz *et al.*, 1986). Applying the R-K equation of state to Eq. (4), we have

$$
ln f_i = ln X_i + ln P + \frac{b_i}{b}(Z-1) - ln(Z-B) - \frac{A}{B}\left[\frac{2\sum_{j=1}^{N} X_j a_{ij}}{a} - \frac{b_i}{b}\right] ln\left(1+\frac{B}{Z}\right) \tag{9}
$$

which is valid for both vapor and liquid phase. With further manipulations of equation of state, the mixture compressibility factor Z can be solved from the following equation.

Table 1.1 Critical Constants and Acentric Factors of Pure Components

	Tc (K)	Pc (bar)	$\bar{v}_c$ (cm^3/mol)	Zc	ω
Oxygen	154.6	50.4	73.4	0.288	0.025
Hydrogen	33.2	13.0	65.1	0.306	−0.218
Helium	5.19	2.27	57.4	0.302	−0.365

Table 1.2 Effective Critical Constants and Acentric Factor of the Helium for the Quantum-Gas Mixing Rules

	Tc (K)	Pc (bar)	$\bar{v}_c$ (cm^3/mol)	ω
Helium	10.47	6.76	37.5	0.0

$$Z^3 - Z^2 + (A - B - B^2)Z - AB = 0 \tag{10}$$

where

$$A = \frac{aP}{R_u^2 T^{5/2}}, \qquad B = \frac{bP}{R_u T} \tag{11}$$

In addition, analytic characterization of critical and supercritical evaporation and combustion is required when the LOX surface reaches the critical mixing state. In treating critical and supercritical processes at pressures greater than the critical pressure of oxygen, the LOX surface is remained at its mixing critical state while the regions below and above the surface are in the state of compressed liquid ($T < T_{cmp}$) and supercritical vapor ($T > T_{cmp}$), respectively. Intrinsically, the LOX exhibits a smooth state transition from liquid to vapor. Furthermore, the vanishing surface tension and the latent heat of vaporization are expected at the interface. The liquid- and vapor-phase compositions are identical under the critical equilibrium conditions.

Based on the above discussion, the key step in the numerical calculation is to fix constant temperature and species-concentration boundary conditions using the values of the mixing critical point once the LOX surface attains the critical state. Thus, the interface boundary conditions are

$$\begin{aligned} T\,|_{x=0} &= T_{cmp}, \\ Y_i\,|_{x=0} &= Y_{i_{cmp}}. \end{aligned} \tag{12}$$

3.2 Implementation of Numerical Code for Phase Equilibrium Model

For a two-component, two-phase system at a given temperature and pressure, Eq. (1) provides two equilibrium equations. According to Eq. (9), the fugacity can be expressed as follows (Lin, 1989).

$$\begin{aligned} ln f_i^{(v)} &= ln X_i^{(v)} + ln P + \frac{b_i}{b^{(v)}}(Z^{(v)} - 1) - ln(Z^{(v)} - B^{(v)}) \\ &\quad - \frac{A^{(v)}}{B^{(v)}}\left[\frac{2\sum_{j=1}^{N} X_j^{(v)} a_{ij}}{a^{(v)}} - \frac{b_i}{b^{(v)}}\right] ln\left(1 + \frac{B^{(v)}}{Z^{(v)}}\right) \end{aligned} \tag{13}$$

$$\begin{aligned} ln f_i^{(l)} &= ln X_i^{(l)} + ln P + \frac{b_i}{b^{(l)}}(Z^{(l)} - 1) - ln(Z^{(l)} - B^{(l)}) \\ &\quad - \frac{A^{(l)}}{B^{(l)}}\left[\frac{2\sum_{j=1}^{N} X_j^{(l)} a_{ij}}{a^{(l)}} - \frac{b_i}{b^{(l)}}\right] ln\left(1 + \frac{B^{(l)}}{Z^{(l)}}\right) \end{aligned} \tag{14}$$

Two more relations can be obtained from the following identities.

$$X_1^{(v)} + X_2^{(v)} = 1, \qquad X_1^{(l)} + X_2^{(l)} = 1 \tag{15}$$

It is noted that the unknowns in the above phase equilibrium equations are mole fractions ($X_1^{(v)}, X_2^{(v)}, X_1^{(l)}$, and $X_2^{(l)}$) of each species. In this study, the Newton-Raphson iterative scheme was employed to solve the mole fraction distributions in a vapor-liquid equilibrium system. In practice, the four unknowns were updated simultaneously by their corresponding corrections during each iteration. To correlate the governing equations with unknowns, Eqs (13) through (15) were further linearized. For Eq. (13), the linearized form is

$$ln f_i^{(v)^{n+1}} = V_{i0} + \sum_{k=1}^{2} V_{ik} \Delta X_k^{(v)} \tag{16}$$

where $n + 1$ represents the (n+1)th iteration.

$$V_{i0} = ln f_i^{(v)^n} \tag{17a}$$

$$V_{ik} = \frac{1}{X_i^{(v)}}\frac{\partial X_i^{(v)}}{\partial X_k^{(v)}} - \frac{b_i}{b^{(v)^2}}(Z^{(v)}-1)\frac{\partial b^{(v)}}{\partial X_k^{(v)}} + \frac{b_i}{b^{(v)}}\frac{\partial Z^{(v)}}{\partial X_k^{(v)}} - \frac{1}{Z^{(v)}-B^{(v)}}\left(\frac{\partial Z^{(v)}}{\partial X_k^{(v)}} - \frac{\partial B^{(v)}}{\partial X_k^{(v)}}\right)$$

$$- \left(\frac{1}{B^{(v)}}\frac{\partial A^{(v)}}{\partial X_k^{(v)}} - \frac{A^{(v)}}{B^{(v)^2}}\frac{\partial B^{(v)}}{\partial X_k^{(v)}}\right)\left(\frac{2\sum_j X_j^{(v)} a_{ij}}{a^{(v)}} - \frac{b_i}{b^{(v)}}\right) ln\left(1 + \frac{B^{(v)}}{Z^{(v)}}\right)$$

$$- \left[\frac{1}{a^{(v)}}\left(2\sum_j \frac{\partial X_j^{(v)}}{\partial X_k^{(v)}} a_{ij}\right) - \frac{2\sum_j X_j^{(v)} a_{ij}}{a^{(v)^2}}\left(\frac{\partial a^{(v)}}{\partial X_k^{(v)}}\right) + \frac{b_i}{b^{(v)^2}}\left(\frac{\partial b^{(v)}}{\partial X_k^{(v)}}\right)\right] \tag{17b}$$

$$\times \left(\frac{A^{(v)}}{B^{(v)}}\right) ln\left(1 + \frac{B^{(v)}}{Z^{(v)}}\right)$$

$$-\left(\frac{Z^{(v)}}{Z^{(v)}+B^{(v)}}\right)\left(\frac{1}{Z^{(v)}}\frac{\partial B^{(v)}}{\partial X_k^{(v)}} - \frac{B^{(v)}}{Z^{(v)^2}}\frac{\partial Z^{(v)}}{\partial X_k^{(v)}}\right)\left(\frac{A^{(v)}}{B^{(v)}}\right)\left(\frac{2\sum_j X_j^{(v)} a_{ij}}{a^{(v)}} - \frac{b_i}{b^{(v)}}\right)$$

And

$$\frac{\partial X_i^{(v)}}{\partial X_k^{(v)}} = \delta_{ik},$$

$$\frac{\partial a^{(v)}}{\partial X_k^{(v)}} = \frac{\partial \sum_i \sum_j X_i^{(v)} X_j^{(v)} a_{ij}}{\partial X_k^{(v)}} = 2\sum_i \sum_j \delta_{ik} X_j^{(v)} a_{ij},$$

$$\frac{\partial b^{(v)}}{\partial X_k^{(v)}} = \frac{\partial \sum_i X_i^{(v)} b_i}{\partial X_k^{(v)}} = \sum_i \delta_{ik} b_i,$$

$$\frac{\partial A^{(v)}}{\partial X_k^{(v)}} = \frac{P}{R_u^2 T^{5/2}}\frac{\partial a^{(v)}}{\partial X_k^{(v)}}, \tag{18}$$

$$\frac{\partial B^{(v)}}{\partial X_k^{(v)}} = \frac{P}{R_u T}\frac{\partial b^{(v)}}{\partial X_k^{(v)}},$$

$$\frac{\partial Z^{(v)}}{\partial X_k^{(v)}} = \Big[(B^{(v)} - Z^{(v)})\frac{\partial A^{(v)}}{\partial X_k^{(v)}} + (Z^{(v)} + 2B^{(v)}Z^{(v)} + A^{(v)})\frac{\partial B^{(v)}}{\partial X_k^{(v)}}\Big]$$
$$/(3Z^{(v)^2} - 2Z^{(v)} + A^{(v)} - B^{(v)} - B^{(v)^2}).$$

Similarly, for liquid phase

$$ln f_i^{(l)^{n+1}} = L_{i0} + \sum_{k=1}^{2} L_{ik}\Delta X_k^{(l)} \tag{19}$$

And

$$L_{i0} = ln f_i^{(l)^n} \tag{20a}$$

$$L_{ik} = \frac{1}{X_i^{(l)}}\frac{\partial X_i^{(l)}}{\partial X_k^{(l)}} - \frac{b_i}{b^{(l)^2}}(Z^{(l)} - 1)\frac{\partial b^{(l)}}{\partial X_k^{(l)}} + \frac{b_i}{b^{(l)}}\frac{\partial Z^{(l)}}{\partial X_k^{(l)}} - \frac{1}{Z^{(l)} - B^{(l)}}\Big(\frac{\partial Z^{(l)}}{\partial X_k^{(l)}} - \frac{\partial B^{(l)}}{\partial X_k^{(l)}}\Big)$$

$$- \Big(\frac{1}{B^{(l)}}\frac{\partial A^{(l)}}{\partial X_k^{(l)}} - \frac{A^{(l)}}{B^{(l)^2}}\frac{\partial B^{(l)}}{\partial X_k^{(l)}}\Big)\Big(\frac{2\sum_j X_j^{(l)}a_{ij}}{a^{(l)}} - \frac{b_i}{b^{(l)}}\Big)\ ln\Big(1 + \frac{B^{(l)}}{Z^{(l)}}\Big)$$

$$- \Big[\frac{1}{a^{(l)}}\Big(2\sum_j \frac{\partial X_j^{(l)}}{\partial X_k^{(l)}}a_{ij}\Big) - \frac{2\sum_j X_j^{(l)}a_{ij}}{a^{(l)^2}}\Big(\frac{\partial a^{(l)}}{\partial X_k^{(l)}}\Big) + \frac{b_i}{b^{(l)^2}}\Big(\frac{\partial b^{(l)}}{\partial X_k^{(l)}}\Big)\Big] \tag{20b}$$
$$\times\Big(\frac{A^{(l)}}{B^{(l)}}\Big)\ ln\Big(1 + \frac{B^{(l)}}{Z^{(l)}}\Big)$$

$$-\Big(\frac{Z^{(l)}}{Z^{(l)} + B^{(l)}}\Big)\Big(\frac{1}{Z^{(l)}}\frac{\partial B^{(l)}}{\partial X_k^{(l)}} - \frac{B^{(l)}}{Z^{(l)^2}}\frac{\partial Z^{(l)}}{\partial X_k^{(l)}}\Big)\Big(\frac{A^{(l)}}{B^{(l)}}\Big)\Big(\frac{2\sum_j X_j^{(l)}a_{ij}}{a^{(l)}} - \frac{b_i}{b^{(l)}}\Big)$$

Subsequently, the equation of $ln f_i^{(v)^{n+1}} = ln f_i^{(l)^{n+1}}$ is imposed to meet the requirement of phase equilibrium. Thus,

$$V_{i0} + V_{i1}\Delta X_1^{(v)} + V_{i2}\Delta X_2^{(v)} = L_{i0} + L_{i1}\Delta X_1^{(l)} + L_{i2}\Delta X_2^{(l)} \tag{21}$$

The final equations in correction mode are given as follows.

$$\begin{aligned}
\Delta X_1^{(v)} + \quad \Delta X_2^{(v)} &= 0 \\
\Delta X_1^{(l)} + \quad \Delta X_2^{(l)} &= 0 \\
V_{11}\Delta X_1^{(v)} + V_{12}\Delta X_2^{(v)} - L_{11}\Delta X_1^{(l)} - L_{12}\Delta X_2^{(l)} &= L_{10} - V_{10} \\
V_{21}\Delta X_1^{(v)} + V_{22}\Delta X_2^{(v)} - L_{21}\Delta X_1^{(l)} - L_{22}\Delta X_2^{(l)} &= L_{20} - V_{20}
\end{aligned} \tag{22}$$

In calculating the mole fractions of each species, the Gauss method was adopted to solve the resulting nonlinear equations (Eq. (22)). Moreover, either Raoult's law or experimental data can be employed to evaluate the initial mole fraction distribution for the first iteration.

3.3 Verification of the High-Pressure Phase Equilibrium Model

With the afore-mentioned numerical implementation, calculations were conducted for the vapor-liquid equilibria of a binary system including oxygen and helium. Figure 1.7 displays the high-pressure phase equilibrium results for the oxygen/helium system. The predictions are in good agreement with the experimental data of Herring and Barrick (1965) over a wide range of pressure and temperature. Following the same calculation procedure, Fig. 1.8 exhibits a computed O_2/He phase equilibrium diagram at four different pressure levels (5, 30, 50, and 68 atm) which correspond the same testing pressure conditions for the companion experimental works. It was observed that the mole fraction of helium in the liquid oxygen (1.0 − mole fraction of LOX) increases with pressure for a fixed temperature. This tendency clearly indicates that the effect of the ambient gases solubility in the liquid phase becomes more important at high pressures.

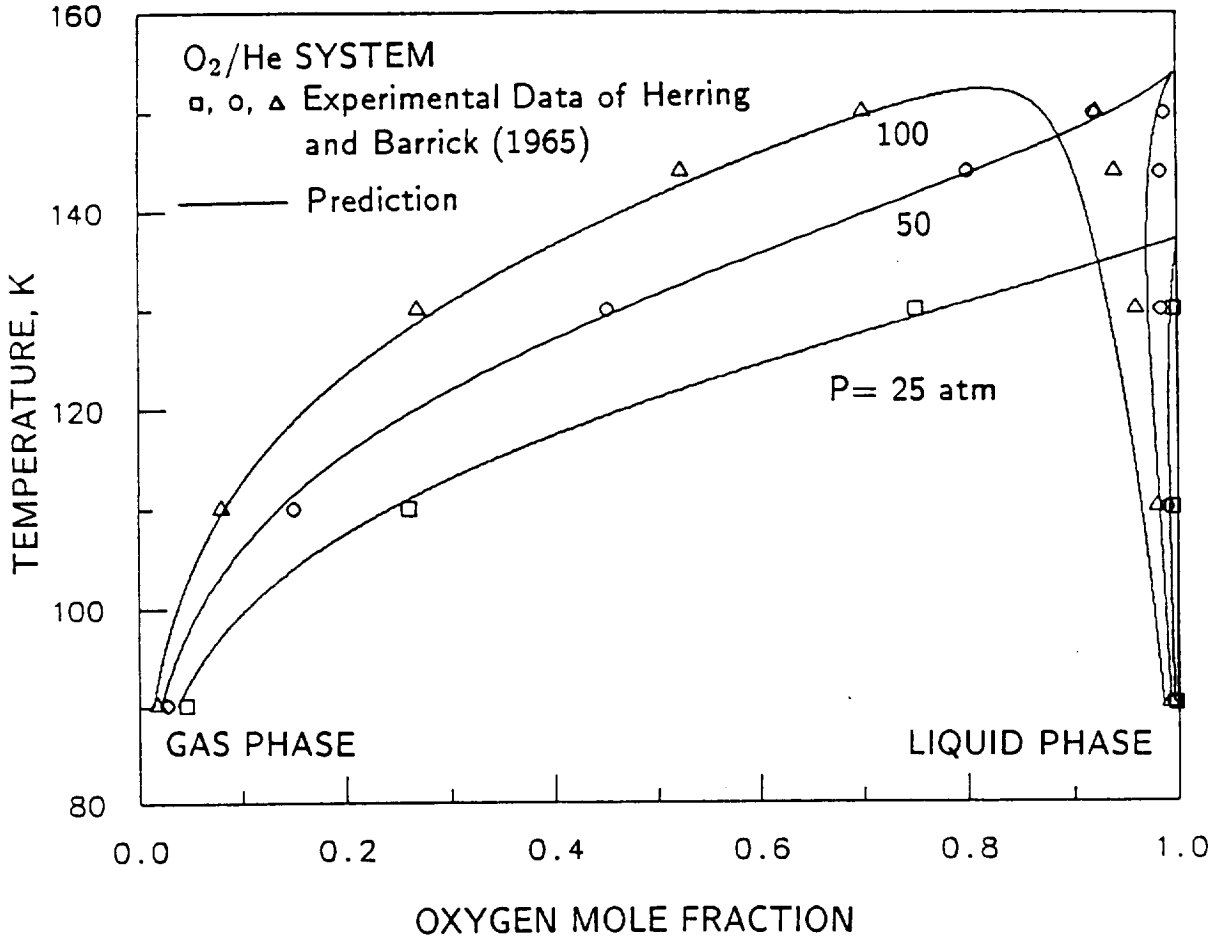

Figure 1.7 Comparison of Computed and Experimental High-Pressure Phase Equilibria; Oxygen/Helium System

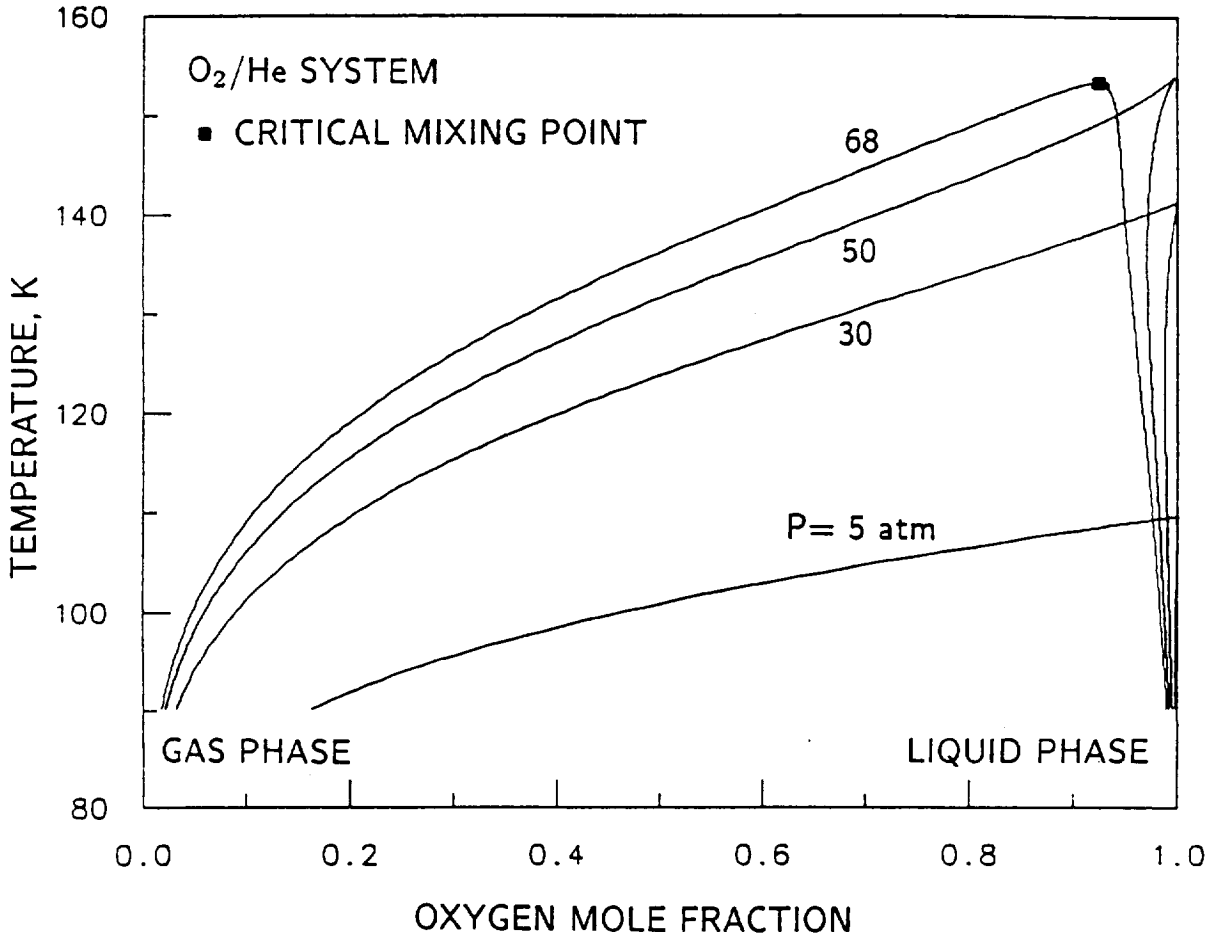

Figure 1.8 Phase Equilibrium Calculations for the Oxygen/Helium System at Various Pressures and Temperatures

3.4 Verification of Numerical Solutions from the Flow Analysis Code

The verification of the numerical code based on the SIMPLE scheme was carried out by comparing the numerical result with the exact solution for the incompressible, steady-state, fully-developed laminar pipe flow. The geometry of the calculated domain was a circular pipe with a length of 20 m and a radius of 1 m. The flow is forced through the pipe by certain pressure gradient. In the calculation, a 30 × 15 grid system has been adopted. The incoming axial flow velocity profile at the inlet was set to be uniform with zero transverse velocity, while the fully-developed condition was applied to the outlet. The assumption of negligible body forces and constant fluid properties were employed in this test case.

Comparison between the calculated and exact solutions of the axial velocity profile (at different radial locations) at the exit of a pipe is in good agreement, as shown in Fig. 1.9. Figure 1.10 shows that the normalized mass residual converges to 10^{-9} within 450 iterations. From the above test case, it is verified that the current numerical scheme is capable of providing accurate solutions as well as reasonable computational efficiency.

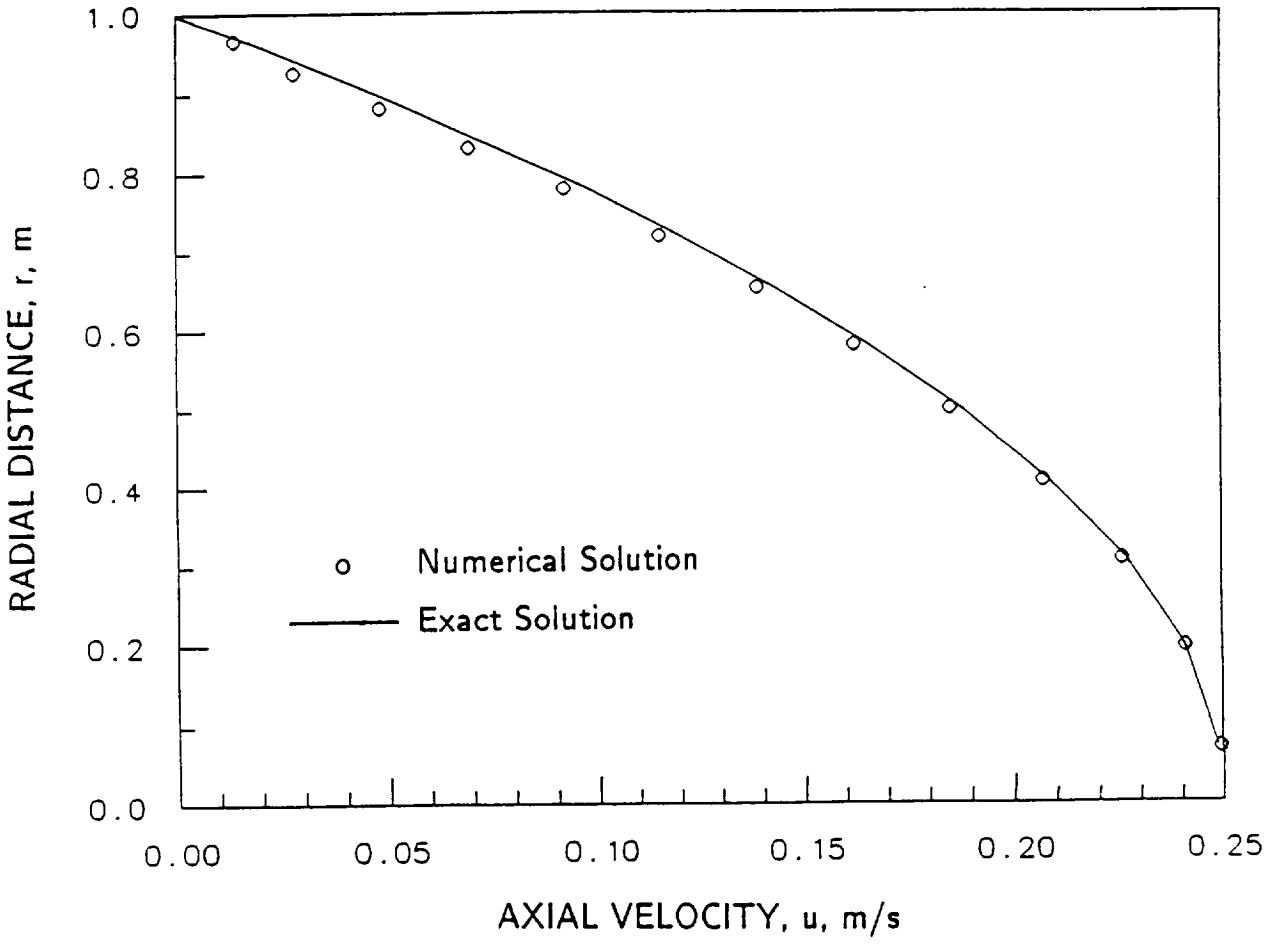

Figure 1.9 Comparison of Exact Solution and Calculated Axial Velocity Profile in a Fully Developed Pipe Flow

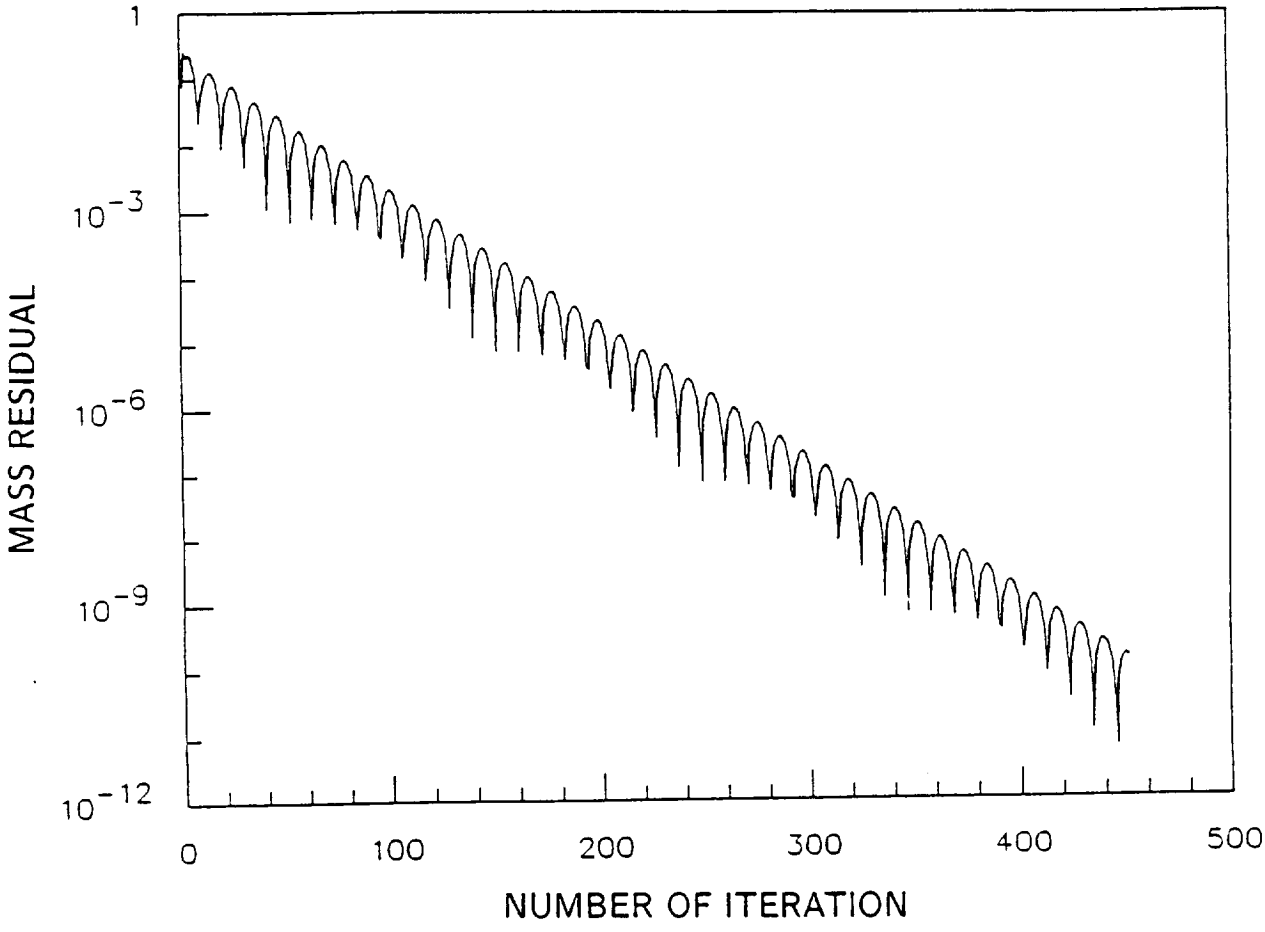

Figure 1.10 Convergence Rate of Normalized Mass Residual for Code Verification

4. DISCUSSION OF RESULTS

The goal of the current investigation is to study the LOX evaporation behavior under high-pressure conditions. Both experimental and theoretical results will be presented and discussed in the following sections.

4.1 Experimental Results

The experimental determination of both evaporation rates and liquid surface temperatures was conducted for LOX liquid strand vaporizing in helium environments. The chamber pressure range varied from 5 to 68 atmospheres. The flow velocity and temperature of the ambient purge gas were maintained at 0.2 cm/sec and at 291 K, respectively.

During the tests, an 150 mm C-mount telephoto lens with 50 mm extension tube was installed in an industrial camera (Panasonic WV-3250) to maximize the viewing area around the opening of the LOX feeding tube (1/4" diameter). With this equipment, the surface situations of liquid oxygen can be closely observed. Generally, it was noticed that the LOX surface exhibits a slightly bulge shape at low pressures. The bulged appearance tends to diminish as the pressure increases. This observation was believed to be caused by the fact that the surface tension becomes weak under high-pressure conditions.

Experimental measurements of steady liquid strand evaporation rates were carried out for a wide range of pressure, as shown in Fig. 1.11. In the pressure range tested in this work, the change in chamber pressure shows a significant effect on the LOX evaporation rate; the evaporation rate increases with raising pressure.

For the surface temperature measurements, the results for various pressure conditions are presented in Fig. 1.12. The boiling point curve for pure oxygen is also shown on the same figure for comparison purpose. In general, the liquid

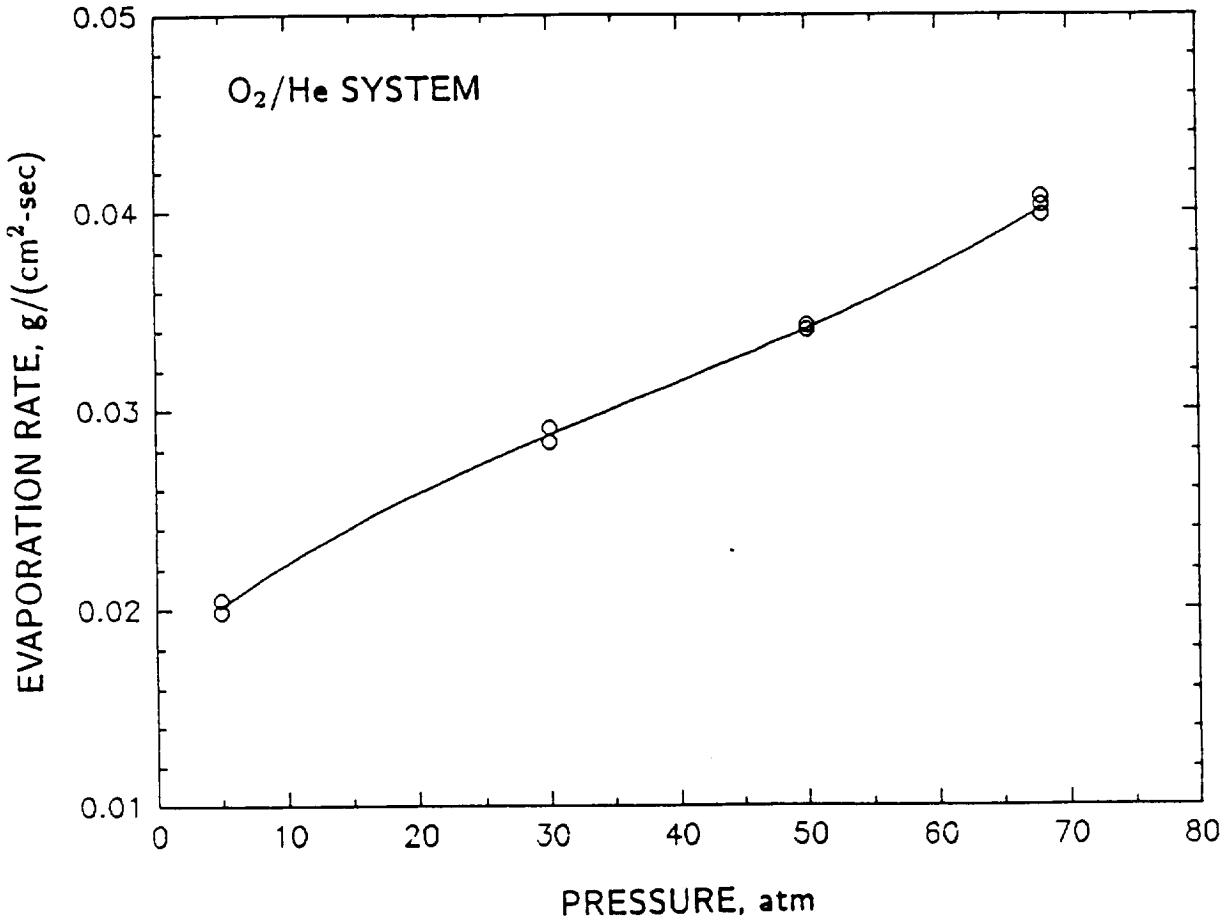

Figure 1.11 Measured Evaporation Rate vs. Pressure for LOX in Helium Environments at Room temperature
(Purge Flow Velocity = 0.2 cm/sec)

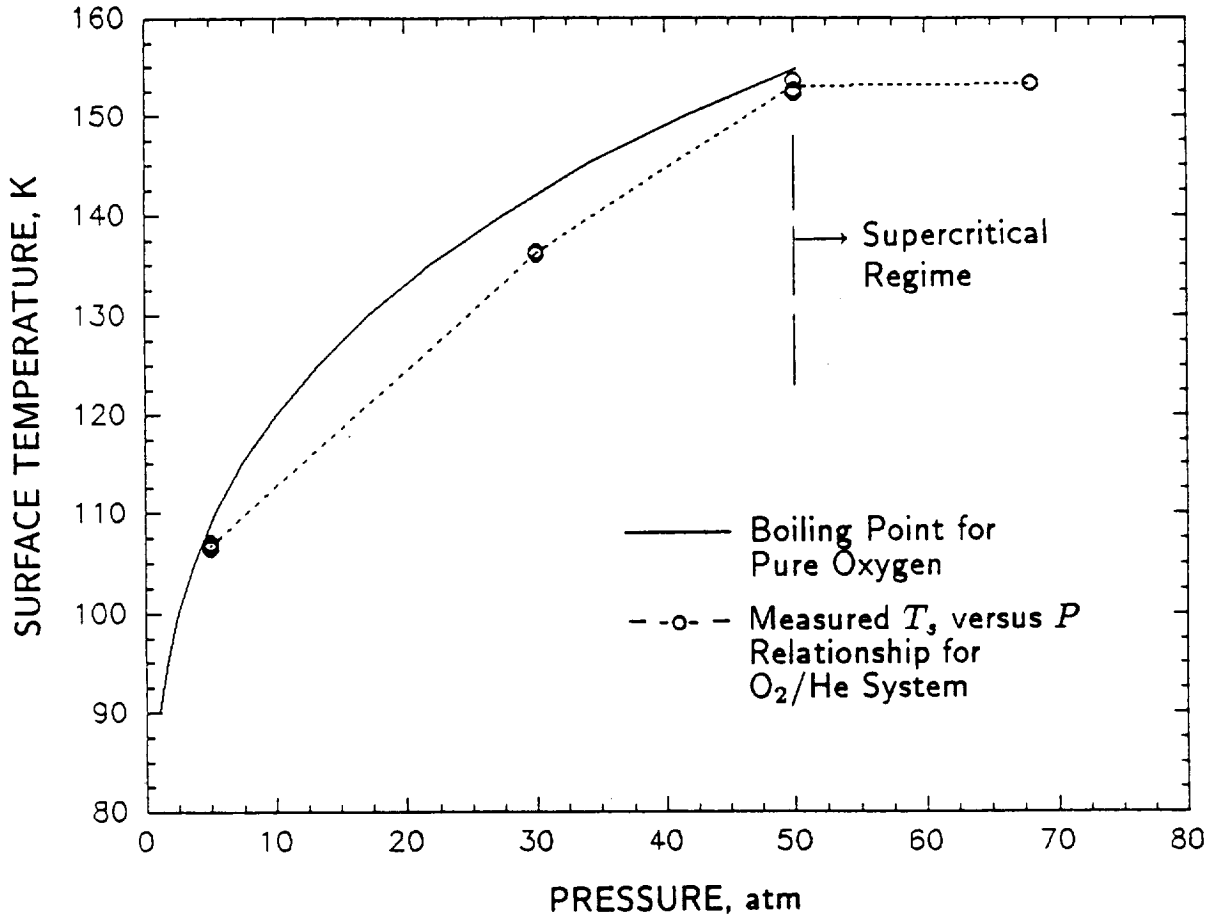

Figure 1.12 Measured Surface Temperature vs. Pressure for LOX in Helium Environments at Room temperature
(Purge Flow Velocity = 0.2 cm/sec)

surface temperature was observed to be slightly lower than the corresponding boiling temperature of pure oxygen at subcritical pressures. In the supercritical regime, the liquid surface temperature is very close to the LOX/He critical mixing temperature calculated by the phase equilibrium model.

To study the mass-transport behavior of LOX during evaporation process, the oxygen concentration profiles were measured using a gas chromatography. During the gas sampling, the quartz microprobe was placed above the LOX surface and aligned with the center line of the LOX feeding tube. Special care has been taken to avoid disturbing the liquid surface by minimizing the sampling rates. The lower limit of the sampling position was 0.85 mm above the LOX surface. When the sampling position was lower than this limit, it was observed that the LOX surface would be disturbed by the probe.

Figure 1.13 presents the center-line oxygen concentration distributions at subcritical (30 atm) and supercritical (68 atm) pressures. The data shown in this figure represent averages of two to four test data. Typically, the values from the individual tests were within 6 % of the average. In the region near the LOX surface, the decreasing slope of the oxygen mole fraction profile at 68 atmospheres was observed to be steeper than that at 30 atmospheres. This phenomenon was attributed to the reduction of convective and diffusive mass fluxes as the chamber pressure was increased. In the downstream region ($x > 20$ mm), oxygen concentration profiles were found to be almost flat.

4.2 Theoretical Results

To validate the theoretical model with the experimental data, calculations were conducted to simulate the evaporation of LOX in a helium surrounding at a chamber pressure of 30 atm. From measured mass flow rates of oxygen and helium, the

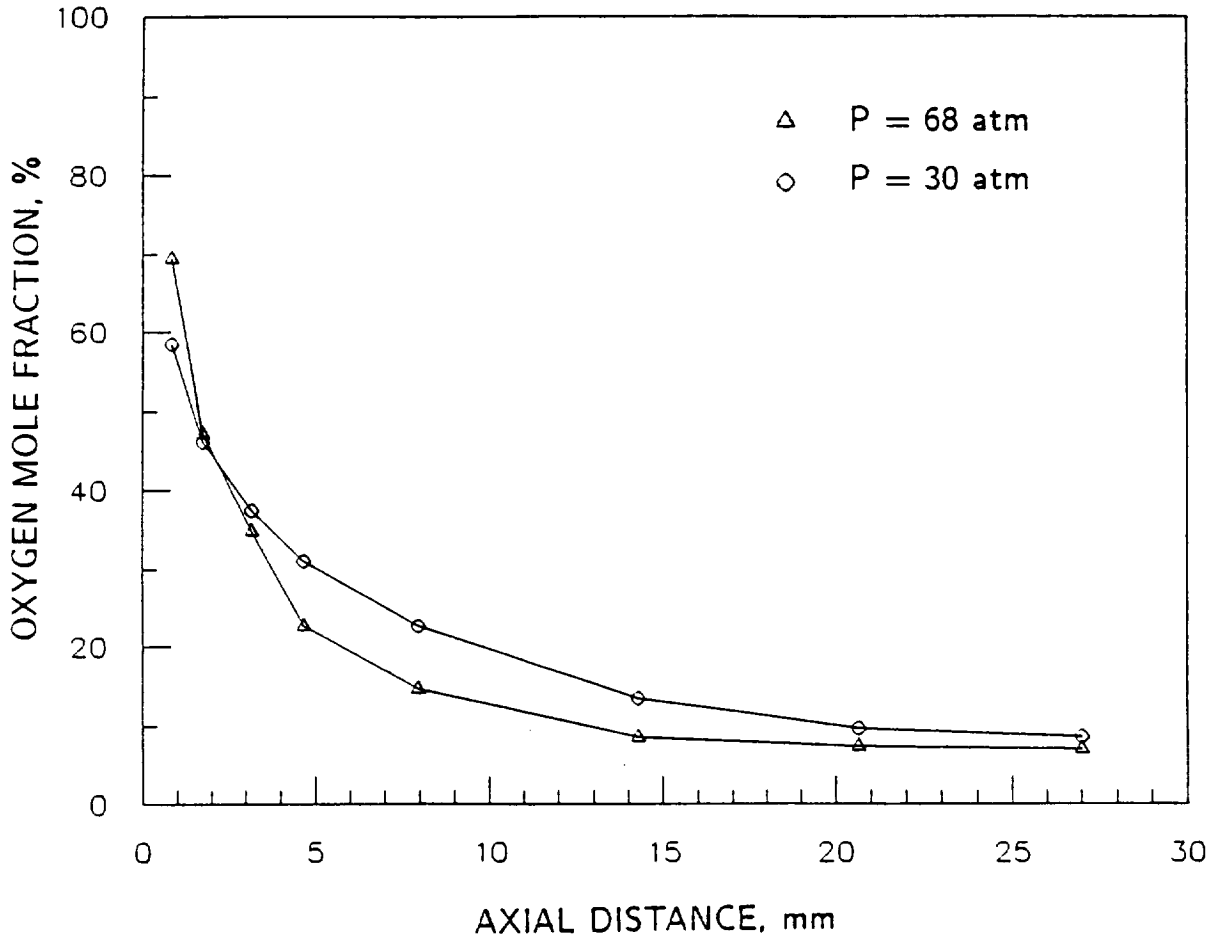

Figure 1.13 Measured Center-line Oxygen Mole Fraction Profiles above the LOX Surface

inflow velocity above the LOX surface and the purge flow was deduced to be 2.61 × 10^{-3} m/s and 2.0 × 10^{-3} m/s, respectively. The temperature measurement of the LOX surface and the helium purge flow showed 136.2 K and 291 K. In addition to the known pressure and surface temperature as input conditions, the oxygen mass fraction at the LOX surface was determined to be 0.981 through the vapor-liquid equilibrium calculations. In this study, the computational domain involved an axial length of 51.3 mm and a radius of 38.1 mm. The radius of the LOX feeding tube was 3.175 mm. The finite difference solutions were performed using a 41 × 29 grid system. The non-uniform mesh size was employed, with both axially and transversely clustered grids, to resolve steep variations of flow properties near the liquid surface and wall. For each calculation, the mass residual of each numerical grid converged to 10^{-6}; the conservation of mass flow rate along the axial direction was within 0.1 %.

The calculated results are presented in terms of temperature and oxygen mass fraction contours, and the center-line oxygen mole concentration profile. Figures 1.14 and 1.15 present temperature and oxygen mass fraction contours with increments of 10 K and 0.05. Due to its diffusion-driven flow nature, both contours display a mushroom cloud distribution. The closely spaced contours near the LOX surface clearly indicate the presence of rapid variations of temperature and oxygen concentration. Figure 1.16 presents the measured oxygen mole fraction data and the predicted center-line temperature and oxygen concentration profiles above the LOX surface. The computed temperature distribution reveals that a significant amount of thermal energy is transferred to the liquid phase for maintaining a steady evaporation rate of LOX. The oxygen concentration profile was observed to drop notably within an axial distance of 10 mm. The calculated result of oxygen mole fraction was also compared with the experimental data. The comparison showed

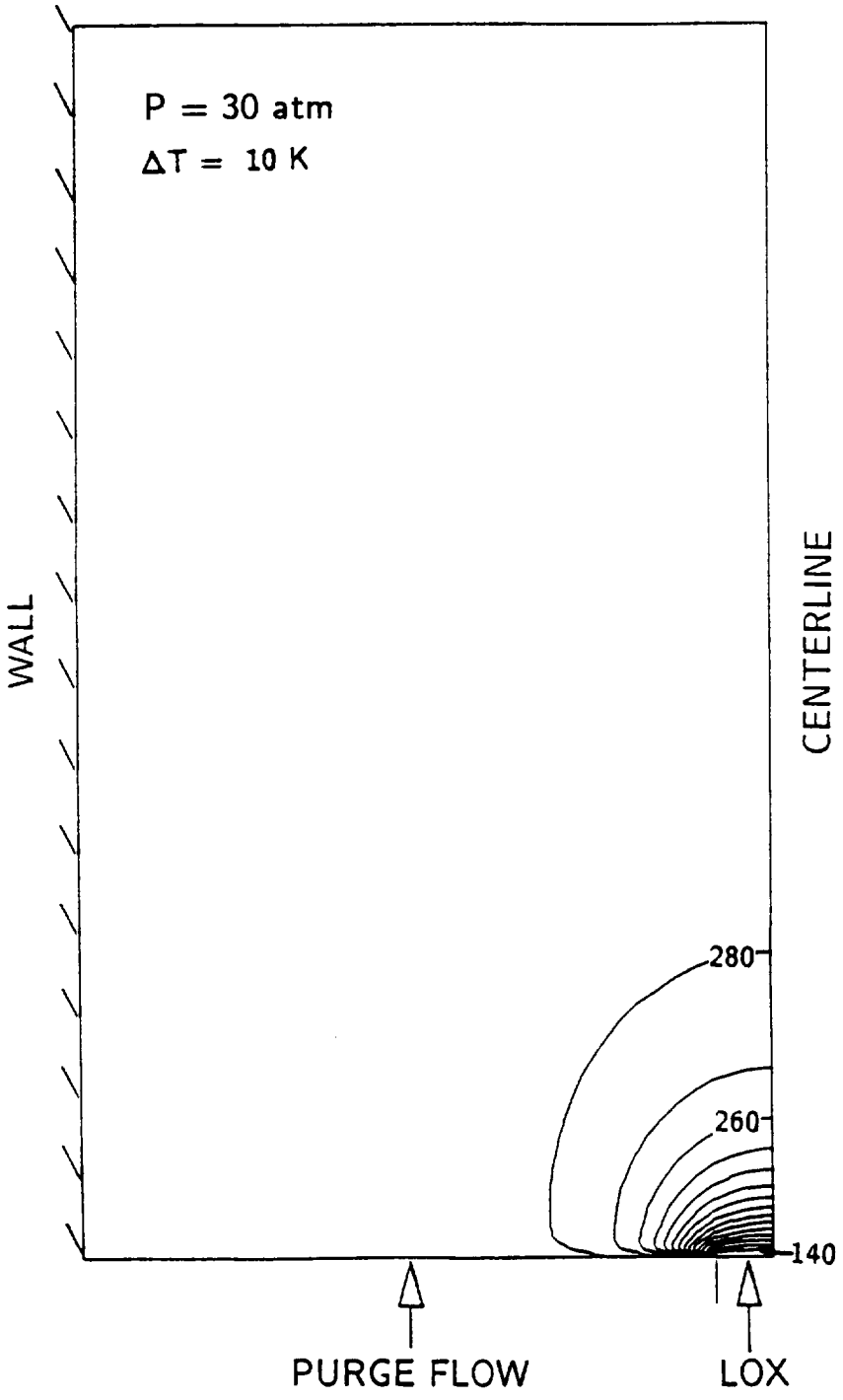

Figure 1.14 Temperature Contour for the Evaporation of LOX in a Helium Surrounding at a Pressure of 30 atm

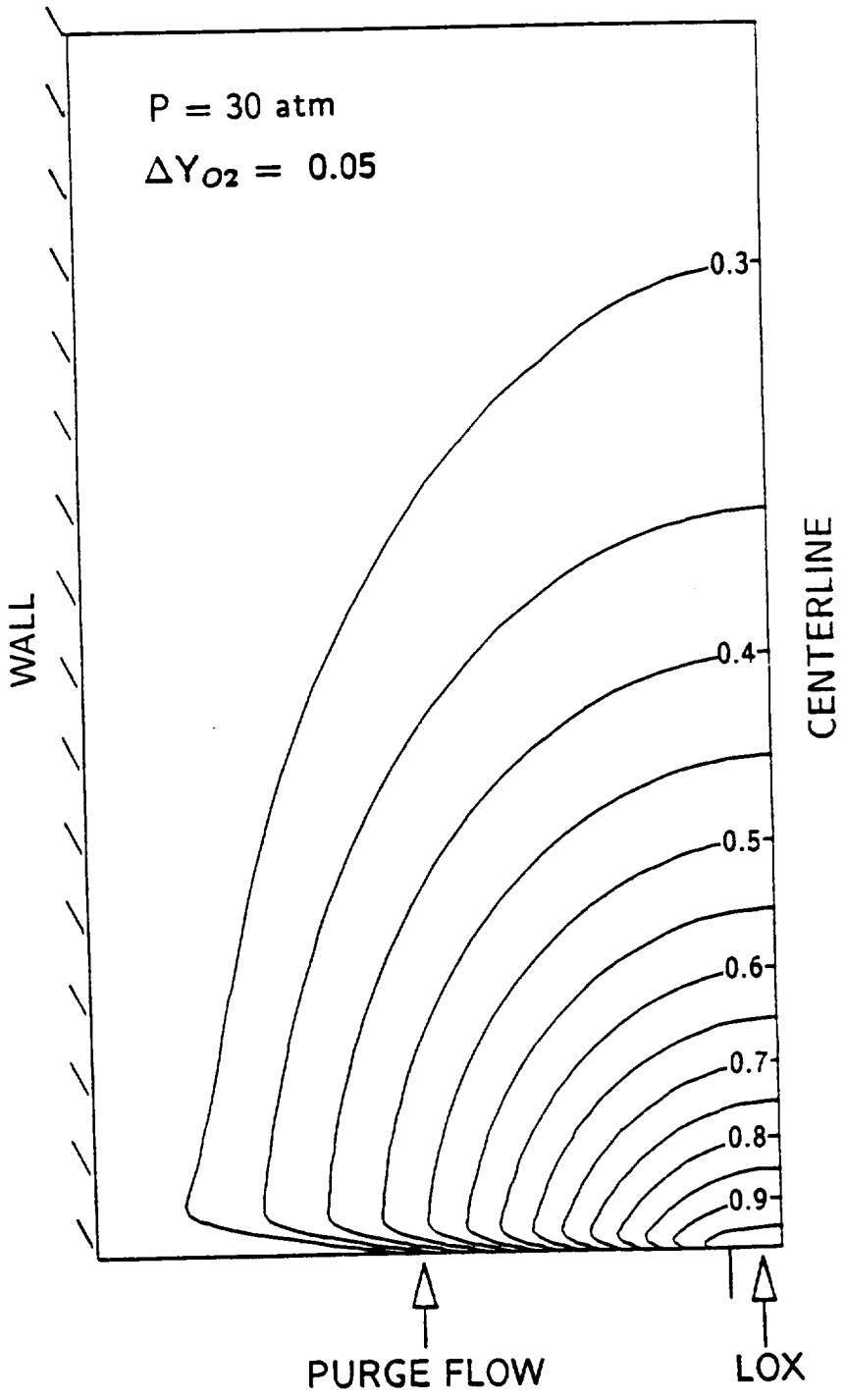

Figure 1.15 Oxygen Mass Fraction Contour for the Evaporation of LOX in a Helium Surrounding at a Pressure of 30 atm

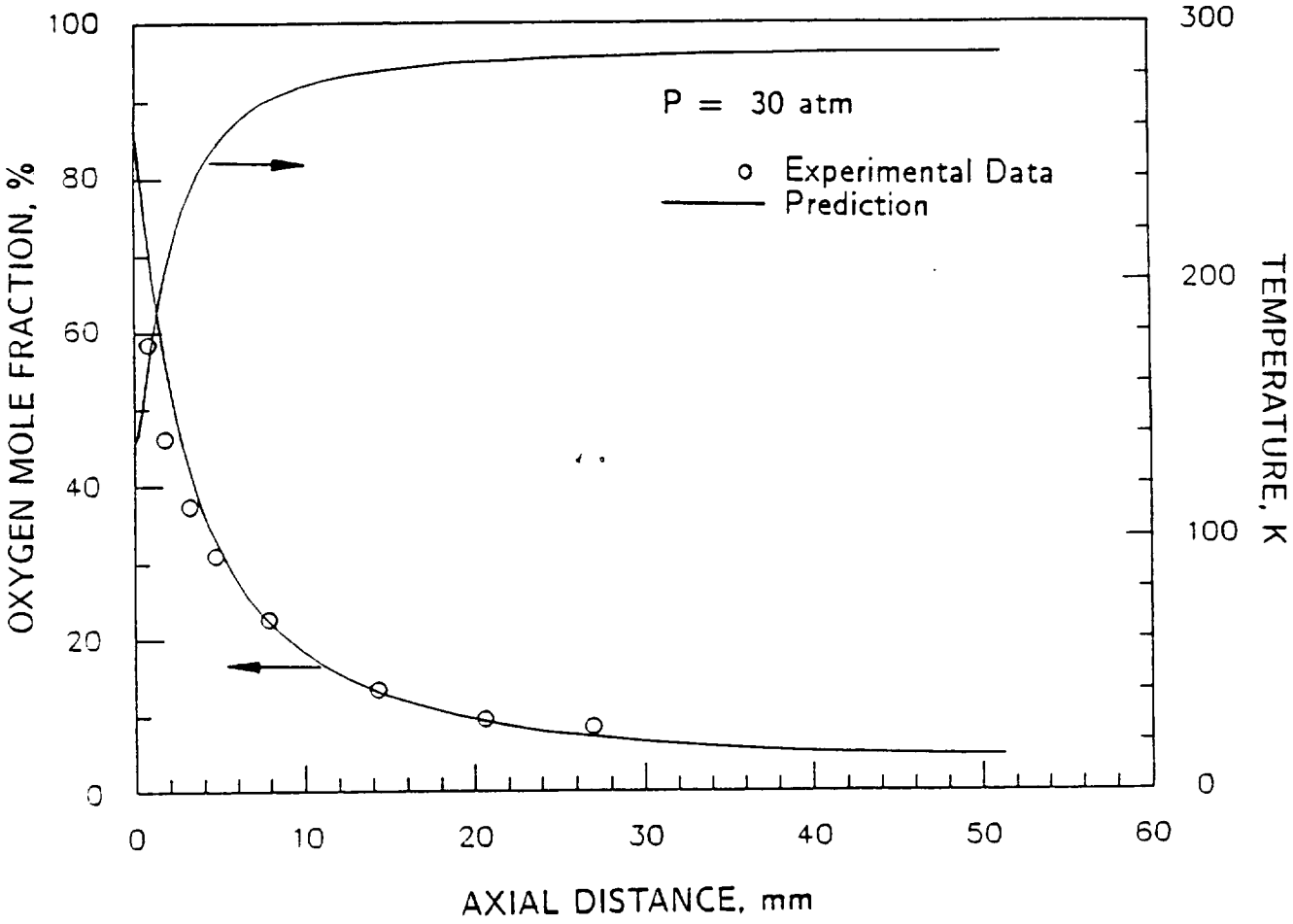

Figure 1.16 Measured Oxygen Mole Fraction Data and Predicted Center-line Temperature and Oxygen Concentration Profiles above the LOX Surface

a reasonably good agreement.

5. OVERALL STATUS

The progress made during this reporting period is summarized as follows. Experimentally, evaporation rate and surface temperature were determined for LOX liquid strand vaporizing in helium environments at pressures ranging from 5 to 68 atm. The gas chromatography analysis was also employed to profile the gas composition above the LOX surface. These data were used to validate the theoretical model under cold-flow conditions. To date, combustion tests have been initiated. Preliminary results showed the establishment of a steady LOX/CH_4/He diffusion flame above the LOX surface. Combustion test results will also be used for model validation in the near future.

Theoretically, a comprehensive theoretical model, consisting of the conservation equations of mass, momentum, energy, and species concentrations for a multicomponent system, has been formulated and solved numerically to study the high-pressure transport behavior associated with the vaporization process. Important features including the solubility of ambient gases as well as variable thermophysical properties have been considered in the model. In addition, a fugacity-based multicomponent thermodynamic phase equilibrium analysis with quantum-gas mixing rules has been established and solved numerically to treat the ambient gases solubility at the interface of a LOX/He system. As a future work, the current computer code will be further extended to simulate the LOX/$H_{2(g)}$ diffusion flame structure.

REFERENCES OF TASK 1

Herring, R. N. and Barrick, P. L. (1965). *Advances in Cryogenic Engineering,* **10**, 151-159.

Lin, J. C. (1989). *Thermodynamic and Numerical Analyses of Multicomponent Fluid Phase Equilibria at High Pressures*, M.S. Paper, The Pennsylvania State University.

Prausnitz, J. M., Lichtenthaler, R. N., and de Azevedo, E. G. (1986). *Molecular Thermodynamics of Fluid-Phase Equilibria*, Prentice-Hall Inc., Englewood Cliffs, New Jersey.

Reid, R. C., Prausnitz, J. M. and Poling, B. E. (1987). *The Properties of Gases and Liquids*, 4th Ed., McGraw-Hill, New York.

Yeh, C. L. (1991). *Measurement of Ignition and Surface Temperatures of Boron*, M.S. Paper, The Pennsylvania State University.

APPENDIX A

OPERATIONAL PROCEDURE FOR LOX/H_2 COMBUSTION TESTS

OVERALL SETUP

Power System

1. Plug the two power strips on the test rig into a shielded extension cable and plug the extension cable into the electric outlet.
2. Turn on the two power strips which are mounted on each side of the test setup. This will activate a hydrogen leak detector and provide power to the solenoid valve, the carrier demodulator for a Validyne pressure transducer, the mass flow meters, and four thermocouple readouts.

Gas Supply System

1. Connect one end of the helium purge line to the high pressure regulator on a helium bottle and the other end to the inlet purge tube.
2. Connect one end of the hydrogen purge line to the high pressure regulator on a hydrogen bottle and the other end to the hydrogen inlet tube.
3. Connect one end of the oxygen line to the oxygen bottle pressure regulator and the other end to the oxygen inlet tube located on the test rig. The flow rate of this line can be well controlled by a micro-metering valve. After introducing gaseous oxygen into the system, the oxygen will be condensed as it passes through the liquid nitrogen bath, and enters the test chamber as a liquid.

Liquid Nitrogen Supply System

Caution: Extreme care must be exercised in use of liquid nitrogen. Due to its cryogenic nature, LN_2 will cause severe burns when in contact with exposed skin. It is recommended that the operator takes the appropriate safety measures, namely, the use of gloves and goggles when handling liquid nitrogen related hardware during the fill operation of the nitrogen bath.

1. Connect the flexible hose to the liquid nitrogen dewar and insert the dispensing end into the nitrogen tank.

Electronic Control/Monitor Systems

1. Calibrate the Validyne pressure transducer and the carrier demodulator.
2. Connect the demodulator to the pressure transducer and mount the transducer to the test chamber.

3. Connect one end of the BNC cable to the back of demodulator and the other end to the IBM PC/AT computer.
4. Turn on the demodulator.
5. Attach the solenoid control cable to the computer.
6. Turn on the computer.
7. Logon to the pressure control program and perform a function check on the solenoid valve.
8. Turn on oxygen deficiency monitor (the reading should be a value of 20.9).
9. Check hydrogen leak detector (a green light should be activated).
10. Connect each thermocouple to its respective readout if not already connected.
11. Turn on the mass flow meter power supply/readout box.

Camera

1. Position the video camera in front of the test chamber window.
2. Connect the camera to the VCR recorder and the recorder to a video monitor. The monitor should be visible to an operator standing in front of the control panel.
3. Insert a labeled video cassette into the recorder and turn on the recorder.
4. Turn on the camera and monitor.
5. Set the test information (i.e. title, date, test number, etc) on the picture for future reference. This is done on the camera.

Control Panel

1. Prior to start, open the helium needle valve and leave the hydrogen needle valve closed for evaporation tests.
2. Make sure all pressure gages read zero and thermocouple readouts indicate a realistic room temperature.
3. Close the purge valve.

Ignition System

1. Install the nichrome-wire ignitor assembly and check its electric resistance (typically 3.5 ohm).
2. Set the switch of the power supply to OFF position and then connect ignitor assembly to the power supply.

SETUP CHECKLIST

1. Both power strips are on.
2. Thermocouple readouts give temperature readings (TCs are working properly).
3. Oxygen, hydrogen and helium lines are securely connected to their inlets on the setup.
4. Liquid nitrogen bath is ready to be filled in LN_2.
5. Computer interface is complete; i.e. data lines, and BNC cables are connected.
6. Demodulator is on.
7. Mass flowmeter indicator is on.
8. Camera is in position and engaged.
9. Proper needle valve settings on the control panel have been chosen.
10. Ignitor is in place.

TEST PROCEDURE

1. Enter the pressure level into the IBM PC/AT pressure control program and initiate the solenoid control sequence. The pressure level is entered as a predetermined demodulator voltage.
2. Briefly open the oxygen regulator and purge the oxygen feed line with a pressure of 50 psig.
3. Close the purge valve.
4. Gradually fill the cooling tank with liquid nitrogen until the liquid reaches a level of 1−2 inches from the top. During this operation the temperature readouts for LOX inlets 1 and 2 should drop to $-196.5°C$. This provides a means by which to judge whether the oxygen line is submerged by the liquid nitrogen bath.
5. When the nitrogen bath is full, check the oxygen regulator to ensure the oxygen bottle pressure exceeds that of the chamber pressure by about two times.
6. Open oxygen regulator and adjust the pressure until the desired mass flow conditions are met. The micro-metering valve on the test setup should be wide open to accelerate the condensation of O_2 in the feeding tube.
7. Check the high pressure helium regulator to ensure the delivery pressure of the helium exceeds the chamber pressure by about two times.
8. Pressurize the chamber and adjust the mass flow rate of He with the helium needle valve located on the control panel.
9. Turn on the camera and begin recording.

10. When desired chamber pressure is achieved, and liquid oxygen is flowing from the feeding tube, decrease the LOX mass flow by adjusting the micro-metering valve on the oxygen inlet line until a stable, stationary level of LOX is maintained at the exit of the feeding tube.
11. Exit test cell and close the door. All personnel should be outside the cell during ignition sequence.
12. Activate ignitor by turning on power supply. Adjust the output current of power supply until nichrome wire is white hot.
13. Introduce hydrogen into the chamber (wait for 5 seconds).
14. If ignition is successful, turn off power supply, and begin data acquisition.
15. If no visible ignition occurs within 5 seconds, remain outside test cell, turn ignitor off and close hydrogen supply while allowing test chamber to be purged with helium for 2 minutes.
16. Make proper needle valve adjustments to increase hydrogen mass flow.
17. Repeat procedure 11 through 15 until successful ignition occurs.

SHUT-DOWN PROCEDURE

1. Close the hydrogen supply (flame will extinguish).
2. Close the oxygen supply and purge the test chamber with helium for 2 minutes.
3. Open the exhaust valve to depressurize the system.
4. Disconnect ignitor assembly from the power supply.
5. Turn off camera.
7. Stop the computer program for pressure control.
8. Turn off Demodulator.
9. Turn off mass flowmeter indicator.
10. Turn off oxygen deficiency monitor.
11. Turn off two power strips on the test rig.
12. Inspect and clean the chamber components.

Task No. 2

DENSE SPRAY AND MIXING OF LIQUID JETS EMANATING FROM DOUBLET INJECTORS

K. K. Kuo, F. B. Cheung, R. D. Woodward and M. C. Kline
Propulsion Engineering Research Center
The Pennsylvania State University
University Park, PA 16802

1. INTRODUCTION

Observation of a like-on-like injector element in the near-injector region performed in the previous phase of this project has identified the existence of a high Reynolds number regime in which the pre-impingement jets are fully turbulent and undergoing surface breakup. The new spray regime, which has not been observed by previous investigators, is characterized by the presence of many fine droplets and the disappearance of the well-defined liquid breakup wave pattern in the post-impingement region. It is speculated that a cavitating region may be present within the orifice so that it could induce strong turbulence, leading to an onset of atomization of the jets prior to impingement.

To further investigate the dense spray behavior of the impinging jets in the high Reynolds number regime, experiments have been conducted using Plexiglas injector components for direct internal flow observation. The main objective is to determine under what conditions a cavitating region would form and whether or not the cavitation is responsible for the development of the high Reynolds number spray regime. This part of the Semi-Annual Report describes the procedure and major findings of the injector cavitation study.

2. PROCEDURE FOR INJECTOR CAVITATION STUDY

The major parameter considered in this investigation is the injection flow rate or jet velocity. Figure 1 shows one setup for determining the mass flow rates. A hand value is used to regulate the flow of liquid from the city-water supply line. The pressure is measured using a pressure transducer connected to a PC-based data acquisition system. A shutter is held over a pre-weighed collection bottle until the flow is at the desired pressure drop. The sutter is then removed while a hand held

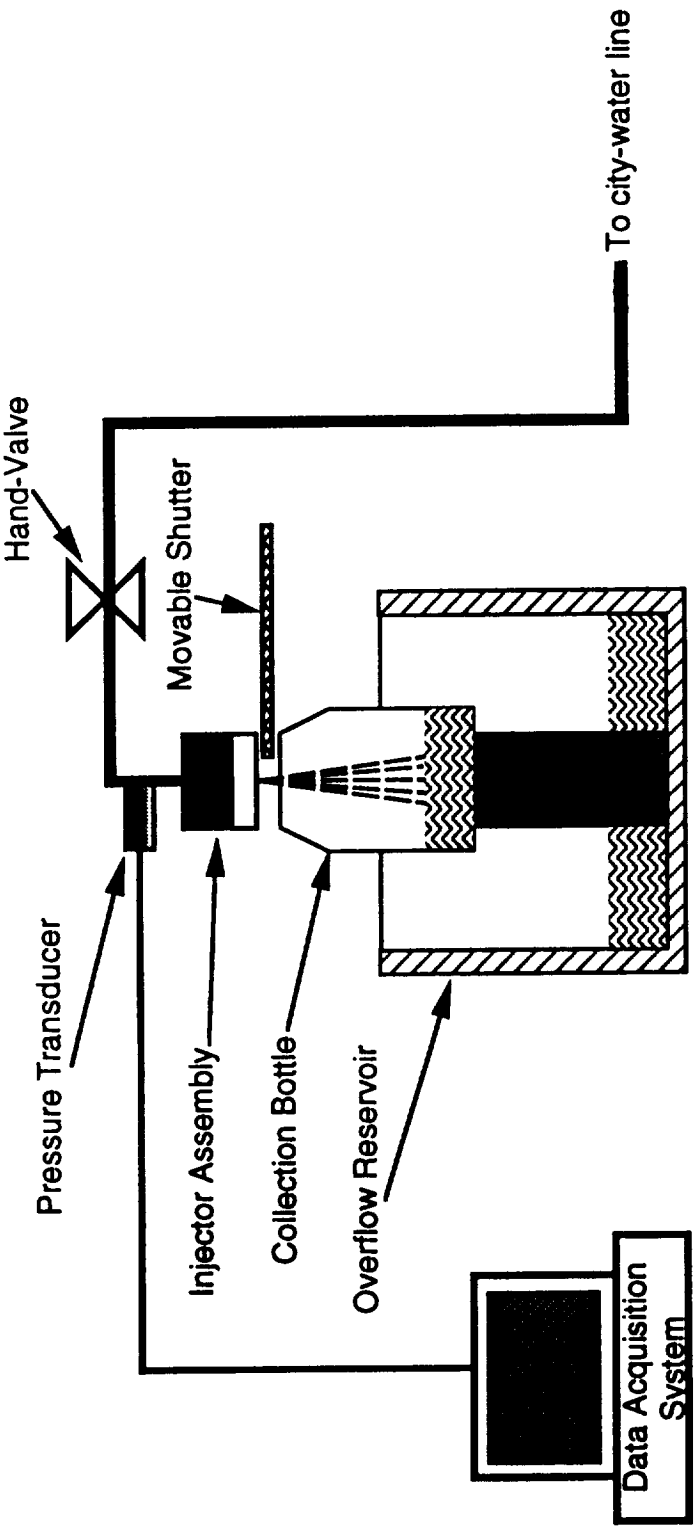

Figure 1. Schematic of Mass Flow Rate Determination

stopwatch measures the time for collection. At the end of the duration, the shutter is moved back into the original position and the time is recorded. The collection bottle is dried with a towel and then the mass of the injected liquid is determined. By knowing the amount of liquid collected, collection duration, pressure drop, properties of the working fluid, and geometry of the injector orifice, the mass flow rate, mean liquid exit velocity and discharge coefficient can be determined. Alternatively, the mass flow rate or velocity at the exit of injector can be obtained from the injection pressure by applying the existing pressure-velocity correlation determined previously for the same injector.

The internal flow within the Plexiglas channel is observed while the behavior of the flow, extent of cavitation, etc., is regulated by controlling the hand valve. This is important since the characteristics of the resulting spray depend greatly on the flow conditions before exiting. Specifically, separated flow induced cavitation can affect the exit flow and possibly its instabilities. One major objective is to visualize the internal flow and relate it to the characteristics of the external flow just after exiting. Another major objective is to make quantitative measurements of the progression and development of the cavitating flow.

The internal flow was visualized by one of two methods using the laser-sheet setup: direct photography with the 35 mm camera or recording of the image to either a S-VHS tape via a Dage/MTI video camera or directly to a Macintosh-based processing system image. The light source for the photographs was either a handlamp placed behind the injector system yielding a shadow graph-type image of the cavitating region, or for better quality photographs the laser-sheet centered on the Plexiglas injector.

3. DATA REDUCTION

The photographs are digitized by a scanner and transferred to the Macintosh for processing. Images taken with the Dage/MTI camera can be directly stored to the image processing system. Also, the images may be replayed in real time with the S-VHS tape or viewed frame by frame with the image processor. This enables the visualization or measurement of flow characteristics.

A digitized background image of the injector channel filled with water was subtracted from the store images for each test run in which cavitation was observed.

This allows for the removal of any minor flaws in the Plexiglas-channel; otherwise these flaws could inhibit certain portions of the field of view. Since the injector channel was present in both photographs being subtracted, the channel must be redrawn with a gray level corresponding to one that would be visible after the processing of the image. A gray level of the cavitation region was chosen. The isophote analysis was used to deduce the cavitation region. The cavitating region appeared as a gray area approximately between 65 and 100 of the 256 gray scales. Finally, the processed image contains mainly the orifice channel and the cavitation region. Measurement of the extent of cavitation or reattachment location (x/L) was then made.

4. RESULTS OF THE INJECTOR CAVITATION STUDY

The cavitation study consists of two parts. The first was a preliminary assessment to determine if a cavitation region existed within the injector channel. Tests were conducted with a Plexiglas channel similar in characteristics to the previous injector only doubled in length and diameter for visualization purposes. The second part was a study to relate the internal flow characteristics to the external flow behavior. This was conducted using a Plexiglas injector with the same (original) dimensions as the 60 degree metal injector previously studied.

4.1 Observation of the Cavitating Region

A photographic study was conducted to observe the internal flow of the channel, using a handlamp to illuminate the Plexiglas test section from behind. Figures 2 a to 2 e show the flow variation with Reynolds number, ranging from $Re_d = 0$ in Figure 2 a to $Re_d = 6.25 \times 10^4$ in Figure 2 e. There is no flow, i.e., $\Delta P = 0$, in Fig. 2 a. Figure 2 b ($\Delta P = 0.4$ psi) depicts a laminar flow throughout the channel and at the exit. Figure 2 c ($\Delta P = 3.7$ psi) shows the inlet to be free of separation (attached flow within the channel), a glassy surface at the orifice exit. The fourth photograph in the series, Figure 2 d ($\Delta P = 14.7$ psi) shows a light gray region near the orifice inlet, signifying the start or onset of cavitation has been reached. Figure 2 e ($\Delta P = 30.05$ psi) shows a broad dark region along the lower wall of the channel. A gray region also appears near the center portion of the port. The broadening of the dark region and the appearance of the gray region signifies that the separation region or cavitation region has developed to a fuller extent. The spray, upon

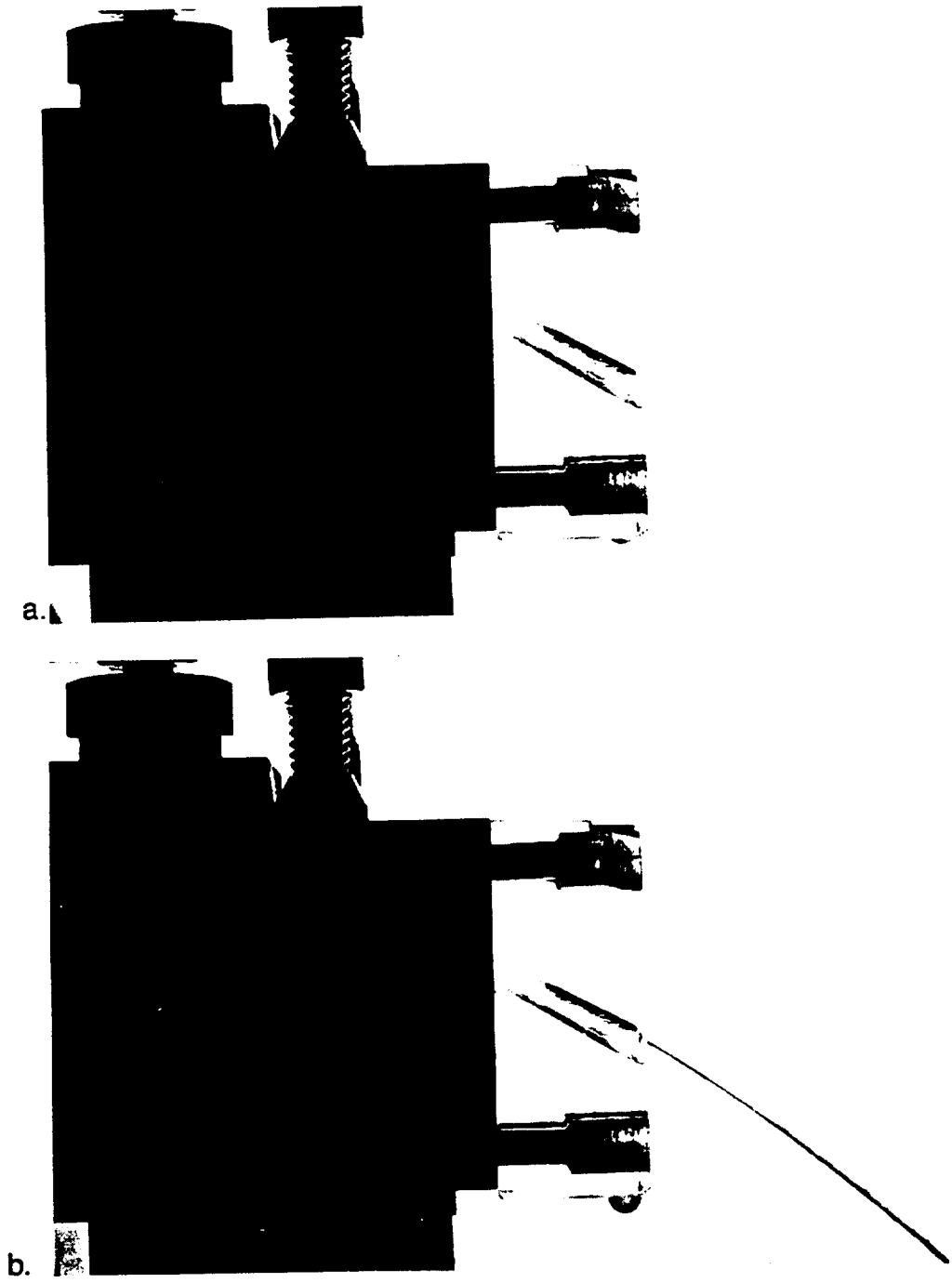

Figure 2. Flow Variation with Increasing Reynolds Number Using the Plexiglas Injector Channel.

(a) $\Delta P = 0.0$ psi., $v = 0.0$ m/s, $Re_d = 0.0$

(b) $\Delta P = 0.4$ psi., $v = 1.82$ m/s, $Re_d \approx 7.21 \times 10^3$

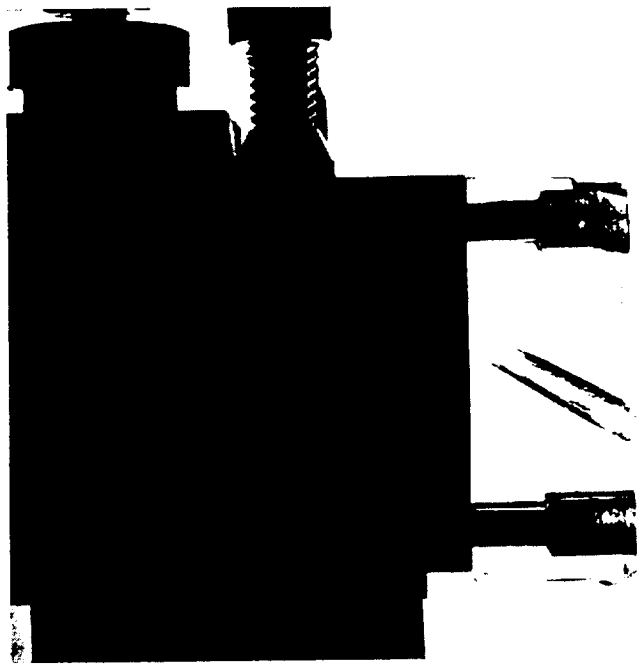

c.

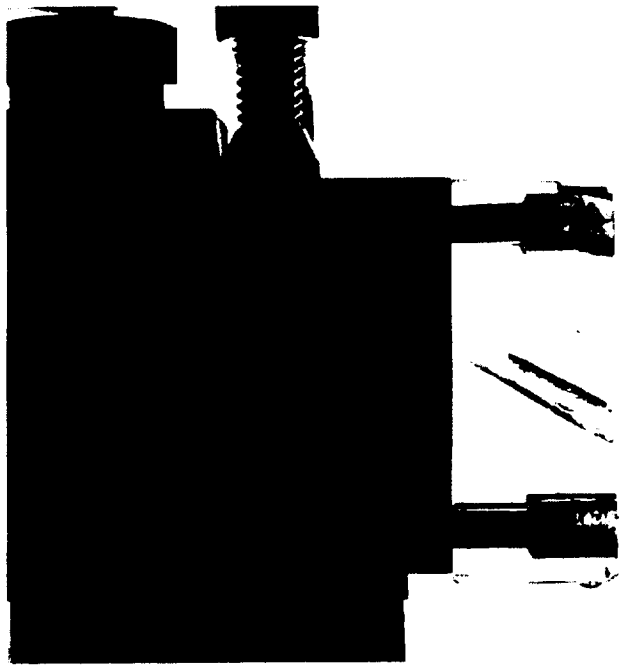

d.

Figure 2 (Cont'd).

(c) $\Delta P = 3.7$ psi., $v = 5.54$ m/s, $Re_d \approx 2.19 \times 10^4$

(d) $\Delta P = 14.7$ psi., $v = 11.04$ m/s, $Re_d \approx 4.37 \times 10^4$

e. 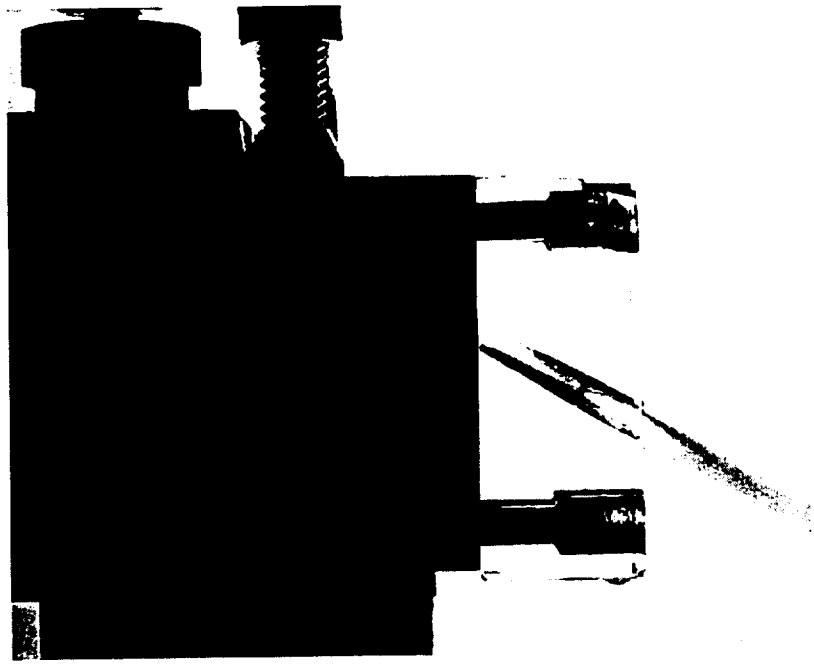

Figure 2 (Cont'd).
(e) $\Delta P = 30.05$ psi., $v = 15.79$ m/s, $Re_d \approx 6.25 \times 10^4$

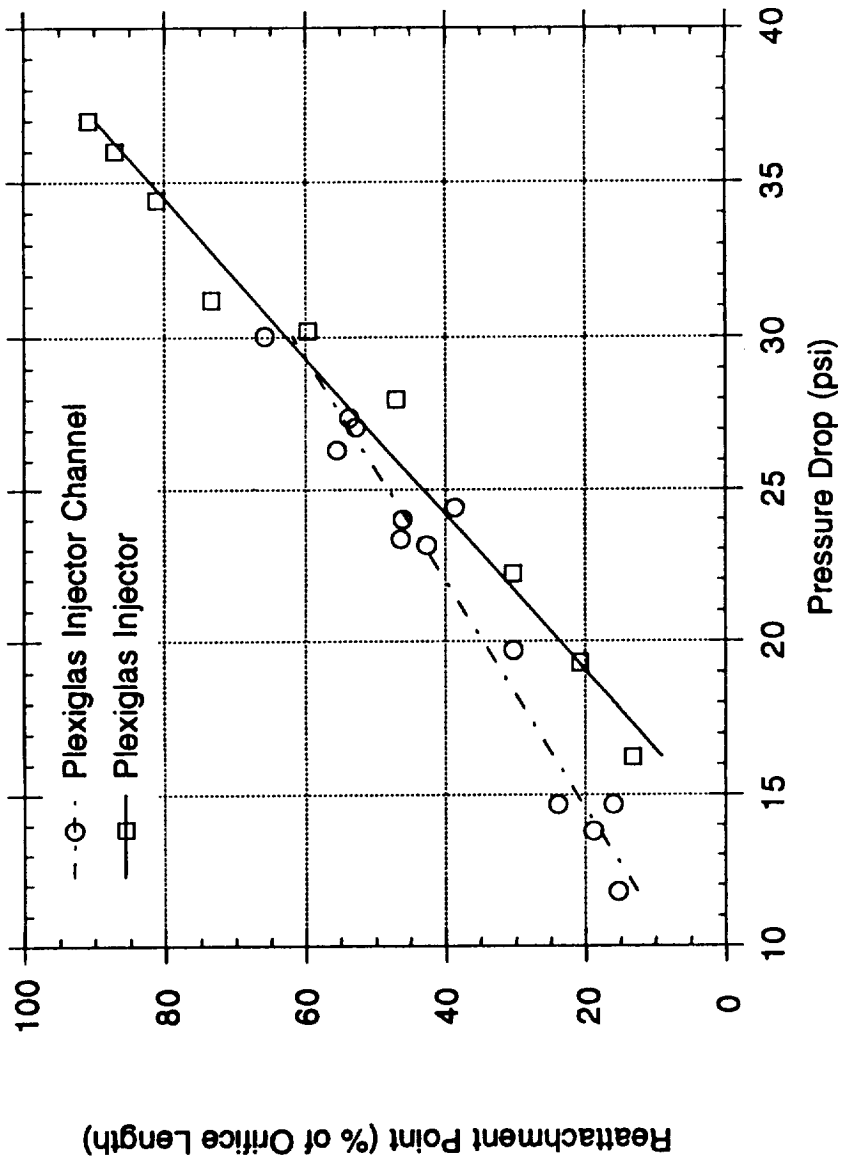

Figure 3. Variation of the Reattachment Point Within the Orifice

exiting the orifice, appears gray and fuzzy as compared to the other photographs.

To determine the reattachment point within the orifice, the laser sheet is also used in a different series of tests to illuminate the cavitating flow within the Plexiglas injector using the Dage/MTI camera with an output line connected to the image processor and video cassette recorder. The result was a stored frame or a motion picture of the cavitation region. The data were processed by the background subtraction method mentioned earlier. The results of the analysis are presented in Figure 3 along with the data for the Plexiglas injector discussed in the next section. The data is plotted as a function of the measured reattachment point in terms of x/L, versus injector pressure drop. A linear relationship was obtained for the cavitation region variation with pressure drop after the point of inception of cavitation.

The cavitation region is formed by the separation region at the channel inlet. The external flow may not immediately be affected by the start of the cavitation. Only when the pressure drop across the injector is beyond a critical level, then the cavitation at the orifice inlet can grow enough in size to influence the external flow. The effect of cavity growth is to increase the turbulence level, which perturbs the flow into atomizing at the exit (jet divergence and loss of glassy appearance).

4.2 Relationship Between the Internal and External Flow

After confirming the existence of the cavitating flow within the injector channel of the scaled mode, the Plexiglas injector was fabricated. The flow within the injector could then be related to the external flow. The injector was studied by three methods: (1) visual observations, (2) still camera photographs, and (3) video images recorded to the image processor.

The photographs and video images were taken with the same procedure used to study the existence of cavitation region inside the injector channel except the back-lighting technique was not used. The pertinent data can be taken with the methods using the laser sheet as the illumination source providing greater detail in the images. The photographs are similar to the images of the injector channel. The point of inception of cavitation was within

±1.0 psi for the two different Plexiglas injector units. The pressure for inception was slightly higher for the injector unit. This implies that the diameter effect was not an important factor for the inception of cavitation. Logically, the pressure for cavitation to occur for this injector geometry strongly depends on the turning angle of the flow. As the impingement angle decreases, the pressure drop required for the flow to cavitate would increase.

Figure 4 shows the sequence of the progression of cavitation from a low pressure drop case, ΔP = 0.3 psi, to a high pressure case, ΔP = 36.3 psi. During the analysis using the Dage/MTI camera, an interesting flow appeared within the orifice channel. Figure 5 shows three digitized images of the injector orifice at a velocity of 1.47 m/s, (Re_d = 2,904), 2.08 m/s (Re_d = 4,122), and 16.14 m/s (Re_d = 31,949). Unlike the cavitating regions seen in previous figures, where the flow looked "fuzzy" or gassy, the flow within the low velocity bubble was very clear (Fig. 5 b). This condition was a rare occurrence. There may be a couple of suitable explanations, possibly, there may have been a pocket of vapor (or air) trapped in the injector that found its way to the low pressure separation region and remained there stably as shown. Another possibility is that the bubble could actually be a cavitation region that remains intact due to the low turbulence level of the liquid flowing over the separation region. In line with this explanation, it seems reasonable that there would be no turbulence enhancement due to cavitation. The bubble did not appear to interfere or disrupt the downstream flow, whereas the typical cavitating region of such extent definitely affected the external flow.

The images were processed in the same manner as before, and the extent of cavitation was measured for different pressure drops. The results were presented in Figure 3 along with the injector channel data. It was observed that the start of the atomization/cavitation regime, corresponding to the appearance of the diverging jet at the exit, occurs for the Plexiglas injector when the cavitation region is between 20 to 30 percent of the length of the orifice. The importance of the cavitation region on the external flow field should not be neglected in this injector design.

The onset of cavitation for the 60 degree Plexiglas injector was seen to be within the fully developed spray regime. Once the cavitation progressed to 20 to 30 percent of the channel length, the exiting flow diverged. The

a.

b.

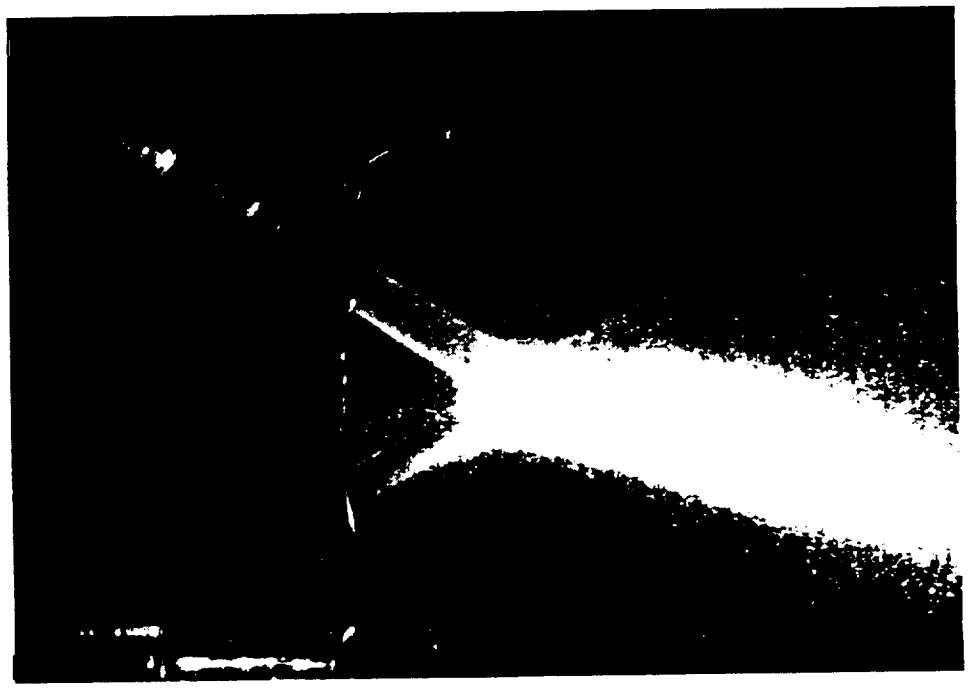

Figure 4 Visualization of the Internal Flow with Increasing Reynolds Number within the Plexiglas Injector.

(a) $\Delta P = 0.3$ psi., $v = 1.47$ m/s, $Re_d \approx 2.90 \times 10^3$

(b) $\Delta P = 13.5$ psi., $v = 9.84$ m/s, $Re_d \approx 1.95 \times 10^4$

c.

d.

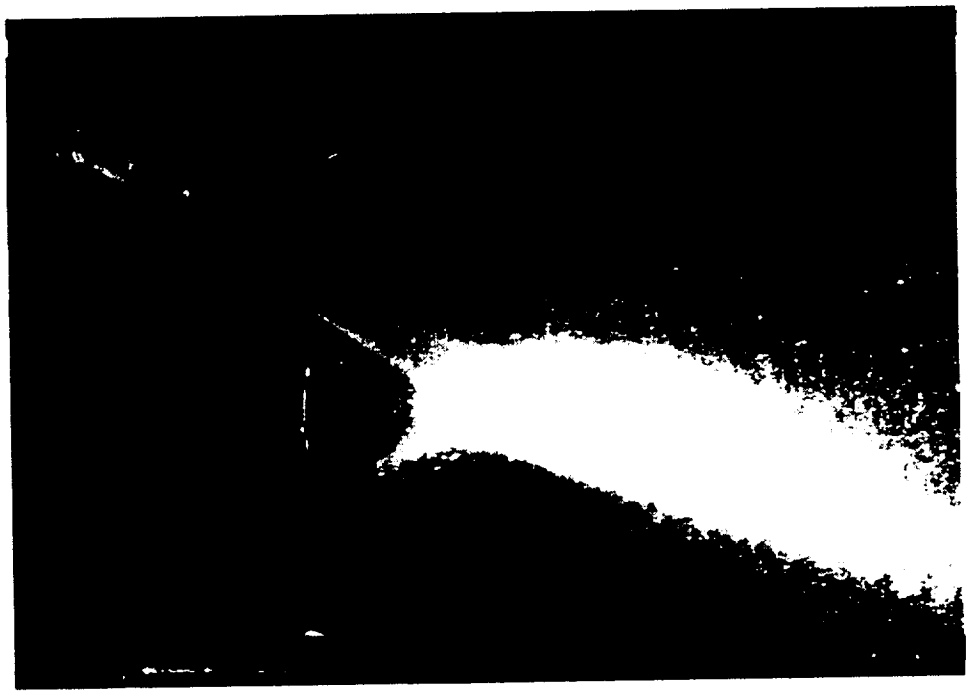

Figure 4 (Cont'd).

(c) $\Delta P = 19.8$ psi., $v = 11.92$ m/s, $Re_d \approx 2.36 \times 10^4$

(d) $\Delta P = 23.8$ psi., $v = 13.07$ m/s, $Re_d \approx 2.59 \times 10^4$

e.

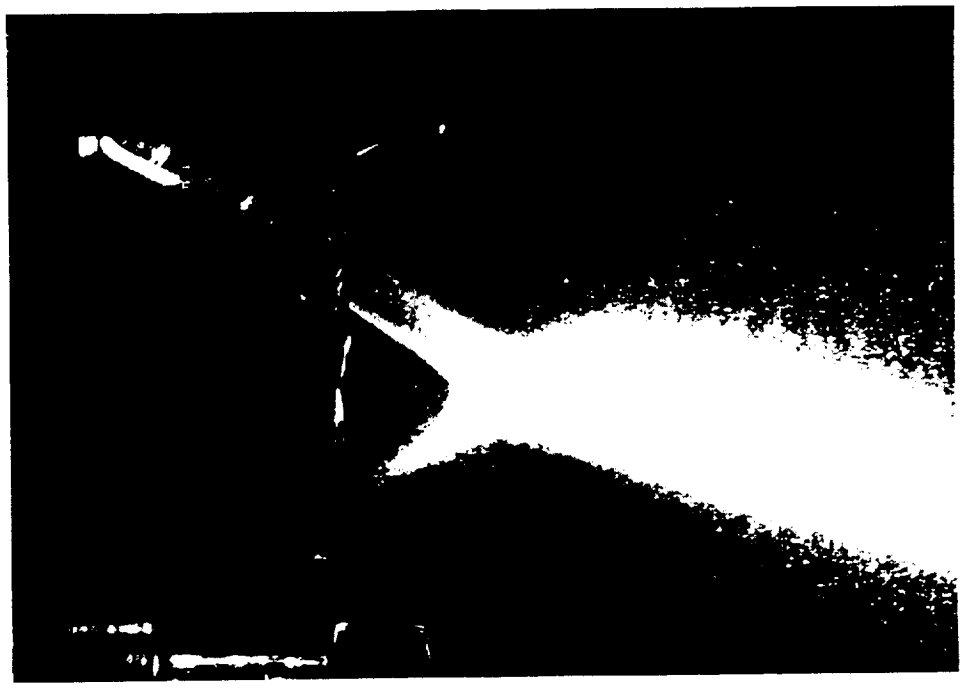

f.

Figure 4 (Cont'd).

(e) $\Delta P = 26.5$ psi., $v = 13.79$ m/s, $Re_d \approx 2.73 \times 10^4$

(f) $\Delta P = 31.1$ psi., $v = 14.94$ m/s, $Re_d \approx 2.96 \times 10^4$

g.

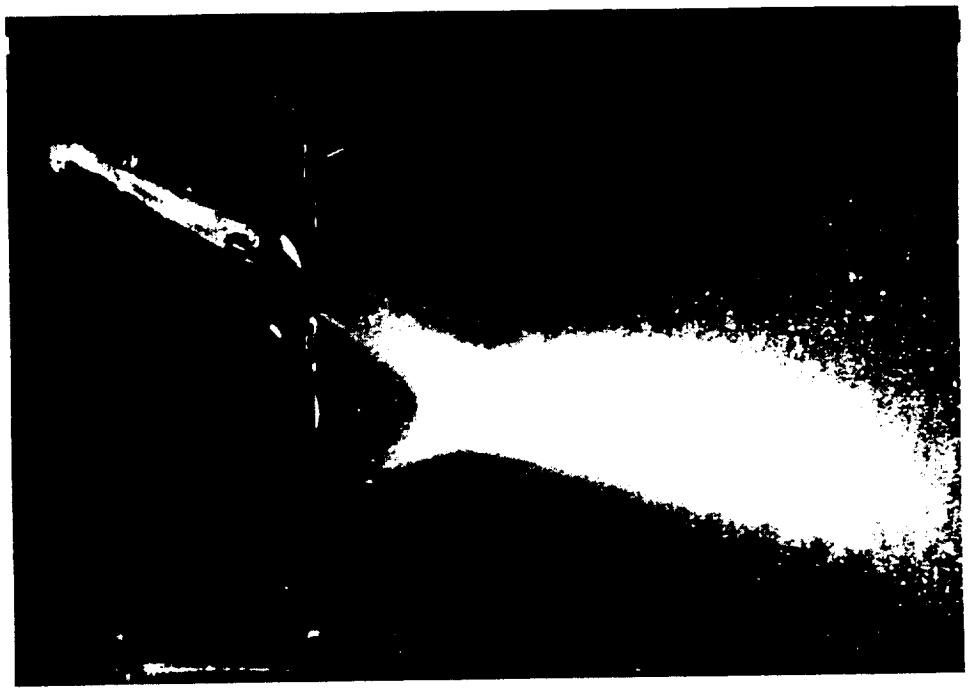

h.

Figure 4 (Cont'd).

(g) $\Delta P = 33.8$ psi., $v = 15.57$ m/s, $Re_d \approx 3.08 \times 10^4$

(h) $\Delta P = 36.3$ psi., $v = 16.14$ m/s, $Re_d \approx 3.19 \times 10^4$

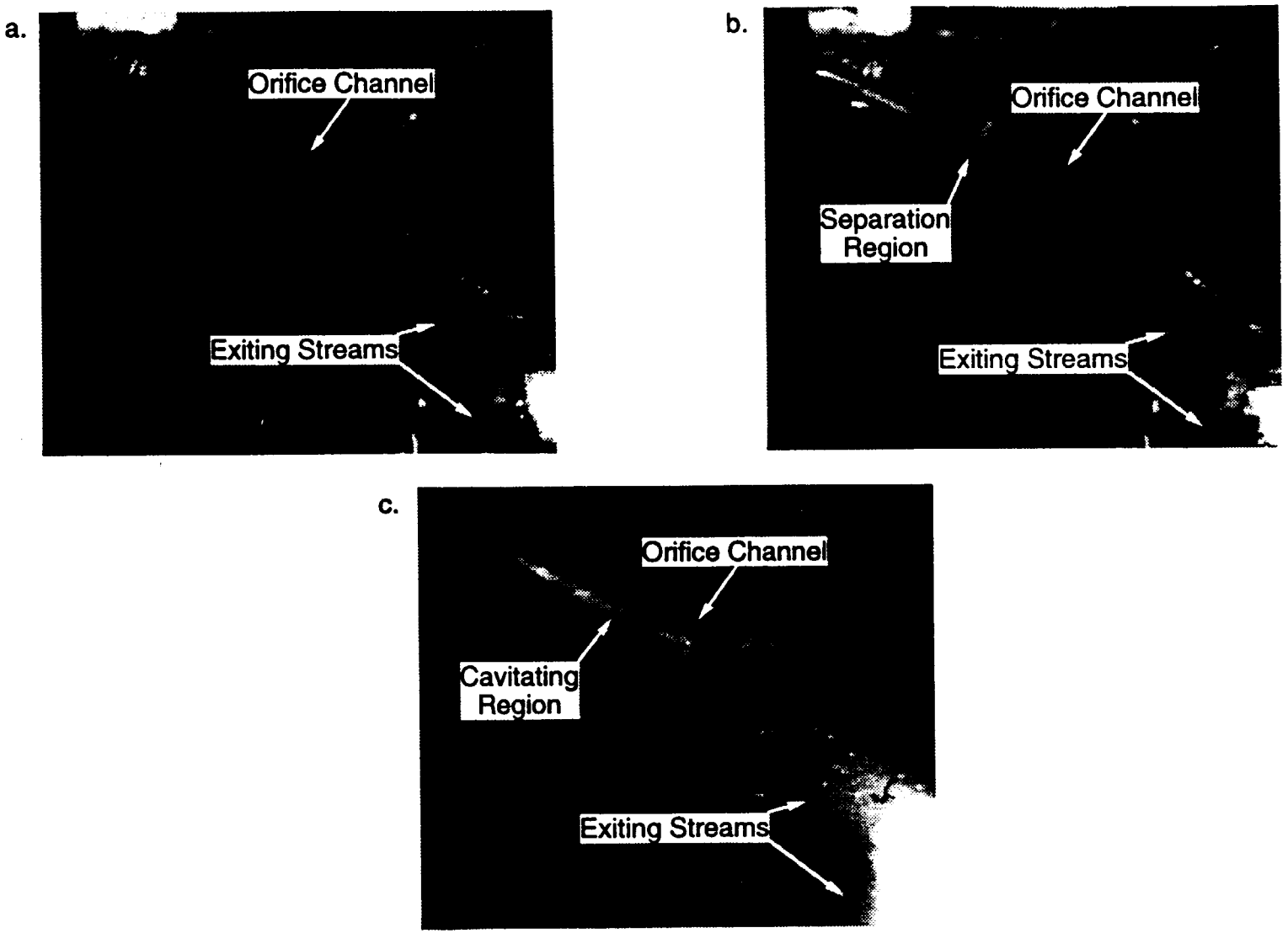

Figure 5 Comparison of Internal Flow Characteristics within the Plexiglas Injector. (a) v = 1.47 m/s, Re_d = 2904, (b) v = 2.08 m/s, Re_d = 4122, (c) v = 16.14 m/s, Re_d = 31949.

cavitation was then able to disrupt the flow by increasing the turbulence level of the stream prior to the point of impingement, causing the distinct change in the resultant spray pattern.

5. REMARKS

A straight unangled orifice (un-inclined with respect to inlet and exit plans) exhibits the typical vena-contracta formation with an axisymmetric cavitation region surrounding the contraction when the critical pressure drop is exceeded. This can lead to hydraulic flip which is characterized by the cavitation vapor exiting the orifice asymmetrically at a location that oscillates in time.

An orifice drilled at an angle to the inlet and exit planes (impingement half angle) causes the flow to separate from the wall adjacent at the sharpest flow turning angle. At sufficient pressure drops for cavitation to occur, the cavitation region remains stably on the same side of the orifice passage without the oscillation characteristic of hydraulic flip. The cavitation, after sufficient development, causes the exiting jets to prematurely breakup before impingement. The premature breakup could be beneficial, especially for a like-on-like injector, for a few reasons. A wider more thoroughly atomized spray fan results after the impingement of the streams compared to the case with no cavitation. Finer droplets are present and more evenly distributed, thus allowing the possibility of increased mixing with a neighboring spray fan. Also the well developed wave pattern, corresponding to a specific breakup frequency, seen in the previously defined "fully-developed" spray regime, is broken down by the introduction of turbulence at a wide range of frequencies. This loss of a dominant characteristic frequency could be helpful in avoiding combustion instabilities in liquid rocket engines.

U. Ed. ENG 91-79